Title

Ecohydrologic processes and soil thickness feedbacks control limestone-weathering rates in a karst landscape

Authors

Dong, Xiaoli
Cohen, Matthew J
Martin, Jonathan B
et al.

Publication Date

2019-11-01

DOI

10.1016/j.chemgeo.2018.05.021

Peer reviewed

Chemical Geology xxx (xxxx) xxx–xxx

Contents lists available at ScienceDirect

Chemical Geology

journal homepage: www.elsevier.com/locate/chemgeo

Ecohydrologic processes and soil thickness feedbacks control limestone-weathering rates in a karst landscape

Xiaoli Dong[a,*], Matthew J. Cohen[b], Jonathan B. Martin[c], Daniel L. McLaughlin[d], A. Brad Murray[a], Nicholas D. Ward[c,e], Madison K. Flint[c], James B. Heffernan[a]

[a] Nicholas School of the Environment, Duke University, Durham, NC 27708, USA
[b] Department of Forest Resources and Conservation, University of Florida, Gainesville, FL 32611, USA
[c] Department of Geological Sciences, University of Florida, Gainesville, FL 32611, USA
[d] Department of Forest Resources and Environmental Conservation, Virginia Polytechnic Institute and State University, Blacksburg, VA 24061, USA
[e] Marine Sciences Laboratory, Pacific Northwest National Laboratory, Sequim, WA 98382, USA

ARTICLE INFO

Keywords:
Chemical weathering
Critical zone
Feedbacks
Patterned landscape

ABSTRACT

Chemical weathering of bedrock plays an essential role in the formation and evolution of Earth's critical zone. Over geologic time, the negative feedback between temperature and chemical weathering rates contributes to the regulation of Earth climate. The challenge of understanding weathering rates and the resulting evolution of critical zone structures lies in complicated interactions and feedbacks among environmental variables, local ecohydrologic processes, and soil thickness, the relative importance of which remains unresolved. We investigate these interactions using a reactive-transport kinetics model, focusing on a low-relief, wetland-dominated karst landscape (Big Cypress National Preserve, South Florida, USA) as a case study. Across a broad range of environmental variables, model simulations highlight primary controls of climate and soil biological respiration, where soil thickness both supplies and limits transport of biologically derived acidity. Consequently, the weathering rate maximum occurs at intermediate soil thickness. The value of the maximum weathering rate and the precise soil thickness at which it occurs depend on several environmental variables, including precipitation regime, soil inundation, vegetation characteristics, and rate of groundwater drainage. Simulations for environmental conditions specific to Big Cypress suggest that wetland depressions in this landscape began to form around beginning of the Holocene with gradual dissolution of limestone bedrock and attendant soil development, highlighting large influence of age-varying soil thickness on weathering rates and consequent landscape development. While climatic variables are often considered most important for chemical weathering, our results indicate that soil thickness and biotic activity are equally important. Weathering rates reflect complex interactions among soil thickness, climate, and local hydrologic and biotic processes, which jointly shape the supply and delivery of chemical reactants, and the resulting trajectories of critical zone and karst landscape development.

1. Introduction

Chemical weathering of bedrock drives the evolution of the critical zone, and contributes to many core critical zone processes, including the flow of energy, cycling of water and carbon, transport and processing of nutrients, and atmospheric dynamics (Rasmussen et al., 2011). Over million-year timescales, silicate bedrock weathering is the most important regulator of atmospheric CO_2 (Berner et al., 1983; Hilley and Porder, 2008), although recent proposals suggest carbonate mineral weathering may also play an important role in controlling atmospheric CO_2 at short time scales (May and Wolfgang, 2010; Torres et al., 2014; Martin, 2017). The suite of hydrologic, ecologic, and geologic mechanisms and feedbacks that govern chemical weathering of bedrock are critical to the geophysical and ecological functions of landscapes.

Bedrock weathering rates are regulated by environmental drivers (e.g., climate) and associated ecohydrologic feedbacks that together influence the supply of acid (principally as carbonic acid produced as water equilibrates with atmospheric and soil CO_2 concentrations), the transport rate (of acid reactants and weathering products), and the path length between acid source (i.e., where CO_2 is produced) and reaction

* Corresponding author.
E-mail addresses: xiaoli.dong@duke.edu (X. Dong), mjc@ufl.edu (M.J. Cohen), jbmartin@ufl.edu (J.B. Martin), mclaugd@vt.edu (D.L. McLaughlin), abmurray@duke.edu (A.B. Murray), nicholas.ward@pnnl.gov (N.D. Ward), mflint@ufl.edu (M.K. Flint), james.heffernan@duke.edu (J.B. Heffernan).

https://doi.org/10.1016/j.chemgeo.2018.05.021
Received 2 November 2017; Received in revised form 27 February 2018; Accepted 13 May 2018

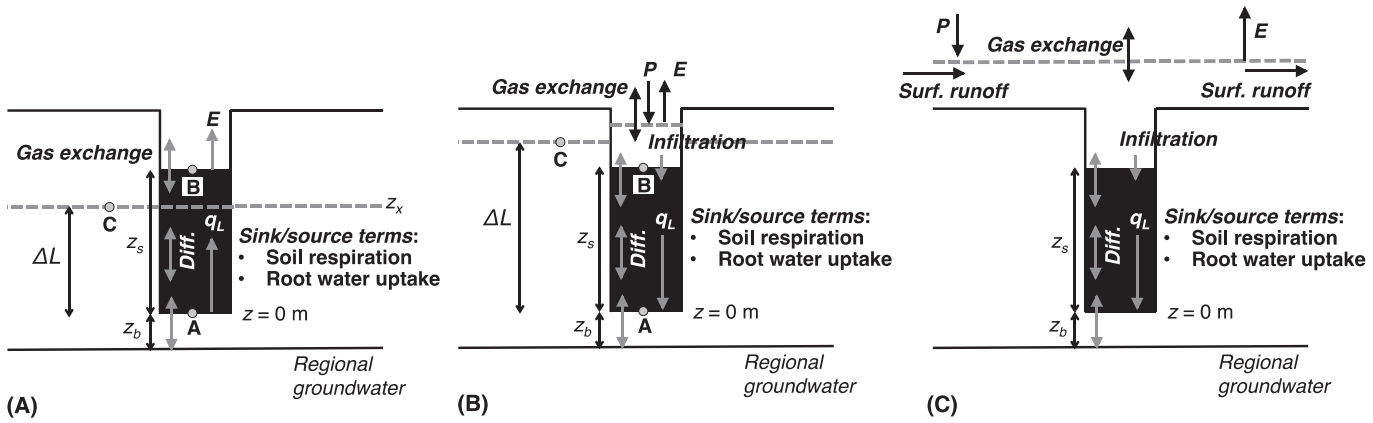

Fig. 1. Schematic of major processes included in the model in two different hydrological states: variably saturated soils (A) and homogeneously saturated soils (B) and (C). (A) When surface water is absent and soil is exposed to atmosphere. We assume in this case that the water table in the depression is the same as water table in the upland catchment. In this state, if rainfall occurs, state (A) can transition to state (B) or (C), depending on the amount of the rainfall. (B) When soil is still inundated by standing water, but upland catchment is exposed: surface runoff = 0. Soil water flux q_L could be either downwards (as demonstrated here, when water table in the depression is higher than water table in the upland catchment) or upwards (not demonstrated here, but when water table in the depression is lower than water table in the upland catchment). (C) When the entire landscape is inundated by surface water: hydrological processes altering surface water table (gray dashed line) include precipitation (P), surface runoff, evaporation (E), root water uptake (in soil column, sink term), and infiltration (top boundary). Soil water flux q_L is downwards. Z_s is soil thickness; Z_b is the elevation difference between soil-bedrock interface and regional groundwater table; ΔL is the difference in elevation between subsurface water in the upland catchment and the soil-bedrock interface; and the in the soil column, there are two major sink/source processes: root water uptake (influences soil water dynamics) and soil respiration (influences soil CO_2 concentration). Bedrock-soil interface is set as the datum plane.

sites. Climate, particularly precipitation, is often considered the most important control on weathering (e.g., Riebe et al., 2004; West et al., 2005). Precipitation supplies weak carbonic acid (i.e., via equilibration with the atmosphere) while also directly controlling soil water dynamics and attendant water and solute transport to and from reaction sites at the bedrock surface (White and Blum, 1995; Gabet et al., 2006; Maher, 2010). Chemical weathering rates may accelerate in tandem with transport up to a threshold where transport is no longer limiting and rates are limited by surface reactions (Steefel and Maher, 2009). Ecohydrologic interactions among climate, vegetation growth, and soil building and respiration can exert additional controls on weathering rates via organic acids and soil CO_2 production, which accelerate weathering by lowering pH (Berner, 1992; Drever, 1994). Estimates of the direct chemical effect of biota on weathering rate vary widely from minor (no more than a factor of 2) to an acceleration of two orders of magnitude (Drever, 1994; Bormann et al., 1998; Moulton and Berner, 1998; Phillips, 2016). In addition to their effect via acid supply, vegetation-climate interactions also influence soil water dynamics, a primary variable controlling CO_2 production, retention, and transport in soil (Moore and Knowles, 1989) and the development of soil cover (Kelly et al., 1998).

Soil thickness exerts important controls on internal weathering feedbacks, and thus on resulting rates, by influencing both the supply and transport (rate and path length) of acidity (Clair et al., 2015; Brantley et al., 2017; Li et al., 2017). Thicker soil cover (i.e., the soil/regolith stratigraphy accumulated on bedrock, including both soil horizons and regolith) enhances establishment and activity of vegetation and microorganisms, which locally elevate CO_2 concentrations and thus acid production that accelerates weathering. This creates a positive feedback between soil cover and weathering rates (Brantley, 2010). In contrast, soil thickening can have a negative feedback on weathering rate by inhibiting solute transport (Kump et al., 2000) and increasing the path length between the source of acidity (i.e., near the surface where root biomass and organic matter are often concentrated) and reaction sites at the bedrock interface. The equilibrium soil cover thickness is thus determined by the relative strength of positive and negative feedbacks on weathering, albeit modulated substantially in some settings by erosion rates, all of which are ultimately controlled by environment conditions (Pelletier and Rasmussen, 2009). A comprehensive understanding of chemical weathering of bedrock, and associated efforts to estimate the timescales and trajectories of critical zone evolution, require an integrated evaluation of these positive and negative feedbacks and their dependence on both internal ecohydrologic processes and external climatic drivers.

Big Cypress National Preserve (BICY, 295 km^2) is a low relief, karst landscape in southwest Florida (USA; Fig. S1). The Tamiami Formation, a limestone bedrock (with ~10% silicate mineral; Petuch and Roberts, 2007), is exposed or near the land surface except in wetland depressions where bedrock elevations are lower and overlying soil cover is thicker. Indeed, soil thickness is significantly correlated with bedrock depth (elevation difference between bedrock and upland matrix; Watts et al., 2014). These wetland depressions are 80–200 m in diameter, about 1.5–2.0 m deep in the center, and regularly dispersed across the landscape with ca. 26% coverage (Watts et al., 2014). During the early Holocene (around 6000 years ago), sea-level rise slowed at an elevation similar to the base of current wetland sediments (Lambeck et al., 2014). BICY is elevated as part of the Immokalee Rise, limiting drainage into the system and resulting in hydrologic regimes largely driven by strong seasonality in precipitation (ca. 70% of rainfall occurs between June and September), as well as hydrologic drainage. Extremely shallow relief (mean landscape slope from north to south is ca. 5 cm km^{-1}) and abundant rainfall lead to prolonged periods of surface inundation, particularly in depressional wetlands (Watts et al., 2012).

With the combination of prolonged inundation, seasonal rainfall, abundant plant production, and evidence of soil accumulation over time on bedrock of different depths, BICY provides an ideal case study to understand controls on chemical weathering of carbonate bedrock. Our goals for this modeling study were to (i) numerically represent a mass balance of carbon and calcium at the scale of individual wetland depressions, and (ii) quantify the time scales over which cypress depressions in BICY developed. We further sought to (iii) investigate the sensitivity of weathering rate to environmental variables in BICY specifically, and carbonate critical zones in general. Lastly, we (iv) assessed the internal ecohydrological feedbacks between soil development and bedrock weathering, and how environmental variables control the strength of such feedbacks.

2. Methods

2.1. Overview

We developed a 1-D (vertical) model to describe calcite dissolution at a weathering front, driven by acidity associated with carbonic acid both from the atmosphere and soil respiration (Fig. 1). The model represents the kinetics of limestone dissolution at the bedrock surface and the precipitation and re-dissolution of calcite in the soil column. It incorporates advective and diffusive mass transport of water and solutes in saturated and variably saturated soils. We allow climatic and eco-hydrologic processes—precipitation, infiltration, evaporation, root water uptake, surface runoff, and local groundwater exchange—to drive temporal variation in soil moisture and saturation, and use a soil water retention module to describe the vertical variation in soil moisture (Fig. 1). As bedrock is weathered, soil accumulates on bedrock. In the model, we assume soil cover thickness to be always 0.65 times the bedrock depth (i.e., soil surface is below the upland exposed bedrock surface by a distance of 35% of bedrock depth), following the empirical observations in BICY by Watts et al. (2014). The model maintains mass balance of water and all solutes and accounts for export of reactants and products via surface and groundwater drainage and for gases (CO_2) via atmospheric exchange. This approach is computationally intensive (a time step of 0.1 s and a spatial resolution of 2 cm), but allows us to estimate absolute rates of limestone dissolution from first principles under the climatic and geomorphic conditions that prevail in Big Cypress. The model, set in BICY, could be transferable to other carbonate critical zones, and comparison with other locations would allow expansion of the understanding of variability of dissolution rate elsewhere.

2.2. Model description

2.2.1. Limestone dissolution at soil-bedrock interface

The kinetics of calcite dissolution and precipitation are determined by three independent rate-limiting processes (Buhmann and Dreybrodt, 1985): (1) kinetics of the dissolution at the interface between solvent aqueous system and limestone bedrock; (2) kinetics of the conversion of CO_2 to carbonic acid; and (3) mass transport of the dissolved species in soil, i.e., Ca^{2+}, HCO_3^-, CO_3^{2-}, CO_2 and H_2CO_3, to and from the weathering surface. We consider these processes in the model simultaneously. We treat bedrock as an infinite source of calcite. Within the soil column, the only source of calcite is reprecipitated material that originates from bedrock dissolution that concentrates elsewhere when soil water content reduces. Reprecipitation of calcite via microbial meditation (Monger et al., 1991) is not considered in the model. The bulk soil is assumed to be composed of organic matter and less soluble minerals (e.g., silicate minerals such as quartz) that remain as a residue after carbonate bedrock dissolution. X-ray diffractograms were measured on wetland soils and bedrock of the surrounding wetlands quantitative modeling of these data using RockJock (Eberl, 2003) show that the Turner River cypress wetland (located in western Big Cypress) soils consist of mixtures of calcite, quartz and smectite, while the soils in the Raccoon point cypress wetlands (located in eastern Big Cypress) consist predominately of quartz. The upland bedrock consists predominately of quartz and calcite, which has Mg contents that range from 2.4 to 5.0%Mg at Turner River locations and from 0 to 5.0%Mg at Raccoon Point sites. Raccoon Point bedrock also has small amounts of aragonite. Soils in wetland depressions are all fine grained. We assume that soil texture is homogeneous vertically—that is, soils at different depth have the same soil hydraulic properties (e.g., saturated hydraulic conductivity, saturated soil water content). When the soil is covered by overland flow, the model also accounts for chemical reactions occurring in surface water.

The reactions responsible for calcite dissolution and precipitation are given by

$$CaCO_3 + CO_2 + H_2O \longleftrightarrow Ca^{2+} + 2HCO_3^- \quad (1)$$

The dissolution rate *DIS* (mmol limestone $cm^{-2}\,s^{-1}$) is described by the PWP equation (Plummer et al., 1978):

$$DIS = \kappa_1(H^+) + \kappa_2(H_2CO_3^*) + \kappa_3 - \kappa_4(Ca^{2+})(HCO_3^-) \quad (2)$$

where the quantities in parentheses are the activities of the corresponding species, and

$$(H_2CO_3^*) = (H_2CO_3^0) + (CO_2) \quad (3)$$

Parameters κ_1, κ_2, κ_3, and κ_4 are temperature-dependent rate constants (definitions and values for parameters used in the model are listed in Table S1). The ion activity is calculated from concentration of the chemical species and its corresponding activity coefficient, the later of which is derived from ion strength (Appendix A). We assume the solution includes only H_2O, H^+, OH^-, Ca^{2+}, HCO_3^-, CO_3^{2-}, $H_2CO_3^*$, $H_2CO_3^*$, and $CaCO_3$. The backward rate constant κ_4 is calculated as (Plummer et al., 1978):

$$\kappa_4 = \frac{K_2}{K_{cal}}\left(\kappa_1' + \frac{1}{(H^+)_s}[\kappa_2(H_2CO_3^*)_s + \kappa_3]\right) \quad (4)$$

where $\kappa_1' = 0.051\ cm\,s^{-1}$ is the limiting value of κ_1 at infinite stirring rate, $(H^+)_s$ and $(H_2CO_3^*)_s$ are the H^+ and $H_2CO_3^*$ activity at the calcite surface. K_{cal} and K_2 are the calcite solubility constant and the equilibrium constant of carbonate ion formation, respectively. The conversion of CO_2 to carbonic acid is pH dependent: at low pH, the dominant reaction is

$$CO_2 + H_2O \underset{k_{-1}}{\overset{k_1}{\rightleftharpoons}} H_2CO_3^0 \rightleftharpoons H^+ + HCO_3^- \quad (5)$$

where k_1 and k_{-1} are reaction constants. The first part of this reaction is slow (half time ~15 s), and the second is so fast that for all cases of interest, $H_2CO_3^0$ and HCO_3^- are in equilibrium. When pH > 7, the dominant reaction is

$$CO_2 + OH^- \underset{k_{-2}}{\overset{k_2}{\rightleftharpoons}} HCO_3^- \quad (6)$$

where k_2, and k_{-2} are reaction constants. Taking into consideration these two pathways, the conversion rate of CO_2 can be described by

$$\frac{\partial CO_2}{\partial t} = -k_1[CO_2] + k_{-1}[H_2CO_3^0] - k_2[CO_2][OH^-] + k_{-2}[HCO_3^-] \quad (7)$$

The quantities in square brackets are concentrations, and they are solved with a system of mass and charge balance equations analytically. Because the conversion from dissolved CO_2 to $H_2CO_3^*$ is slow (first part of reaction in Eq. (5)), dissolution or precipitation will drive CO_2 away from equilibrium with other chemical species. The remaining chemical reactions are fast, and equilibrium between the corresponding species can be and is assumed.

2.2.2. Soil water dynamics and solute transport under different hydrologic states

We considered chemical reactions and mass transport in two primary hydrological states of soil with one additional variant (Fig. 1): (1) variably saturated soil whose upper boundary is exposed to the atmosphere (Fig. 1A), (2) homogeneously saturated soil with possible inundation (i.e., standing water) (upland soil surface is exposed; Fig. 1B) or with overland flow (upland is also inundated; Fig. 1C). We calculated the mean monthly rainfall depth between 2007 and 2017 in South Florida and applied that to the model as the monthly precipitation regime for BICY. The daily rainfall is stochastic (time step for rainfall is a day): the number of rainfall days in a month and the size of each rainfall event (m) is random, under the constraint that rainfall within each month sums up to the mean monthly rainfall. Whether rainfall could generate overland flow depends on the soil water content before the

rainfall event. We assumed that rainfall first fills up the unfilled soil moisture storage capacity in soils, and if there is still remaining rainfall water, it generates overland flow. If the rainfall depth is less than air space in the soil column (e.g., small rainfall events occurring at the end of long dry period when soils are very dry), no overland flow results. When the surface water inundates the entire landscape (Fig. 1C), the water loss paths include surface runoff, evaporation, transpiration (by root water uptake), and slow (constant) groundwater loss to regional groundwater (q_L). As water table continues to lower and surface water only occurs in wetland depressions, surface runoff stops and local groundwater exchange at the soil-bedrock interface can occur in both directions: flowing into soil or away from soil, depending on the local head gradient (described below). Further loss of water—if no rainfall occurs—eventually lowers the water table below the soil surface, at which time the soil transitions from saturated to variably saturated conditions. For variably saturated soil, evaporation at soil surface, root water uptake, and local groundwater exchange (upwards into soil from groundwater) continue to occur, altering the vertical soil moisture profile. We thus model shifts between different hydrological states and specific processes for soil water dynamics and solute transport in each.

2.2.3. Hydrologic State 1: Soil water dynamics and solute transport in variably saturated soils

Soil water dynamics in variably saturated soils. Variably saturated soils are simulated with two soil layers: an unsaturated layer from atmosphere-soil interface to subsurface water table (at z_x, Fig. 1A) and a saturated layer from subsurface water table z_x to soil-bedrock interface ($z = 0$; Fig. 1A). The model simulates soil moisture across the soil profile in 2 cm intervals. We assume homogeneous soils and the model does not include preferential flow of water. Soil water dynamics in the unsaturated layer are described by Richard's equation under the assumption that the gaseous phase of water (vapor) plays an insignificant role in soil water content and that vapor flow due to thermal gradients can be neglected (vapor and heat flows are important for soil water flows in arid regions but can be neglected in BICY; Zeng et al., 2011; Xiang et al., 2012):

$$\frac{\partial \theta_L}{\partial t} = -\frac{\partial q_L}{\partial z} - S = \frac{\partial}{\partial z}\left(K\left(\frac{\partial \psi}{\partial z} + 1\right)\right) - S \tag{8}$$

where q_L is the water flux (flux density of water, $m\,s^{-1}$), θ_L is volumetric water content ($m^3\,m^{-3}$), ψ is the pressure head (m), K is the hydraulic conductivity ($m\,s^{-1}$), z is the spatial coordinate in vertical direction (m; positive upwards), and the sink term S ($m^3\,m^{-3}\,s^{-1}$) represents the volume of water removed per unit time from a unit volume of soil due to root water uptake. Root water uptake is regulated by water stress (Eq. B5 in Appendix B). The soil water content θ_L and hydraulic conductivity K are both functions of pressure head and are described by van Genuchten's (1980) closed form approach, based on the capillary model of Mualem (1976) (Appendix B).

For the saturated layer, q_L can be described by

$$q_L = -K_{sat}\frac{(z_x + \psi(\theta_{L,z_x}) - \Delta L)}{z_x} \tag{9}$$

where z_x (m) is the water table in soils (elevational head; Fig. 1A), $\psi(\theta_L, z_x)$ is the pressure head at the interface of the water table z_x and the unsaturated soil layer, and ΔL (m) is the water table in the upland catchment, which is used to approximate the pressure head at the soil-bedrock interface (Fig. 1A). We assume that when soil is exposed, the water table in soils equals to water table in upland catchment, i.e., $z_x = \Delta L$; therefore, Eq. (9) can be simplified to

$$q_L = -K_{sat}\frac{\psi(\theta_{L,z_x})}{z_x} \tag{10}$$

z_x is prescribed with a periodic function (with amplitude A_{zx}, period $2\pi/B_{zx}$, and vertical shift C_{zx}), to mimic the variation of water table in time in response to evapotranspiration and rainfall and lateral flow between wetland and adjacent aquifer (similar to McLaughlin et al., 2014). We prescribe the model with different periodic functions reasonable for the study site for z_x (we assume a mean water table of 50% of soil thickness) to test the effect of the form of the function on mean annual weathering rate. The choice of parameters A_{zx}, B_{zx}, and C_{zx} has negligible effect on mean annual weathering rate. In the model, we prescribe z_x with a function with period of three months ($B_{zx} = 2\pi/(365 \times 24 \times 3600/4)$), amplitude A_{zx} being 20% of soil thickness, and vertical shift of C_{zx} = soil thickness/$(2 \times 365 \times 24 \times 3600)$ so that the mean annual water table is 50% of soil thickness.

Boundary conditions for the soil water dynamics in variably saturated soils. BICY is located in a region that features a shallow groundwater table (Sullivan et al., 2012). In places of shallow groundwater, the hydraulic gradient between the saturated zone and the root zone could lead to continuous supply of groundwater to soil (Chen and Hu, 2004). Water flux (q_L) at the boundary of saturated–unsaturated transition (the first layer of grid not saturated) is described by

$$q_L(z_x, t) = -K(z_x, t)\left(1 + \frac{\psi(z_x, t)}{dz}\right) \tag{11}$$

where z_x is water table in soil, as described previously (Eq. (10)). Because the water table in the depression never drops below the soil-bedrock interface, the true lower boundary shares the same formula as Eq. (10), and is expressed as

$$q_L(0, t) = -K_{sat}\frac{\psi(\theta_{L,z_x})}{z_x} \tag{12}$$

Water flux across the upper boundary (soil-atmosphere interface) is defined by:

$$q_L(L, t) = E + k_i \tag{13}$$

where E is evaporation rate at the soil surface ($m\,s^{-1}$) and k_i ($m\,s^{-1}$) is the infiltration rate ($k_i = 0$ when there is no surface water). We used a simple linear method (after Laio et al., 2001) to represent the rate of evaporation:

$$E = \frac{\theta_L - \theta_h}{\theta_s - \theta_h}E_p \tag{14}$$

where E_P ($m\,s^{-1}$) is the potential evaporation, and θ_s and θ_h are saturated soil volumetric water content and the hygroscopic point.

Transport of CO_2 in variably saturated soils. CO_2 transport in unsaturated soils occurs in both dissolved and gaseous phases. CO_2 concentration in the soil is governed by convective and diffusive transport, and by CO_2 production (biological respiration and precipitation of dissolved calcium) and/or removal (limestone dissolution). CO_2 transport is described by the following mass balance equation:

$$\frac{\partial(CO2_G\theta_G + CO2_L\theta_L)}{\partial t} = \frac{\partial}{\partial z}\theta_G D_G\frac{\partial CO2_G}{\partial z} + \frac{\partial}{\partial z}\theta_L D_L\frac{\partial CO2_L}{\partial z} - \frac{\partial}{\partial z}q_L CO2_L + R_G + RC_{CO2} \tag{15}$$

where R_G and RC_{CO2} are sink/source terms. RC_{CO2} is CO_2 consumption or production resulting from calcite dissolution or precipitation (Eq. (1)). R_G denotes soil respiration (including both root and microbial respiration). We assume a positive linear relationship between soil thickness and total amount of root dry mass in soil (valid for BICY as detailed in Appendix C). For vertical distribution of root biomass in soil, we assume root biomass density B_r increases exponentially with distance from bedrock-soil interface:

$$B_r(z) = A\left(\frac{blm}{e^{Az_s} - 1}\right)e^{Az} \tag{17}$$

where blm is belowground biomass ($kg\,m^{-2}$; its estimation is provided in Appendix C), z_s is total soil depth (cm), and z is the distance to soil-

bedrock interface (cm). We use $A = 0.02$ for BICY, which results in about 70% of the root biomass retained in the top 0.3 m of a 1 m deep soil for bald cypress (Megonigal and Day, 1992). Eq. (17) is constructed to ensure:

$$\int_0^{z_s} B_r(z)dz = \int_0^{z_s} A\left(\frac{blm}{e^{Az_s}-1}\right)e^{Az}dz = blm \tag{18}$$

The reduction of soil respiration caused by soil water stress follows (Simunek and Suarez, 1993), and is expressed as:

$$f_s = \frac{\log|\psi| - \log|\psi_3|}{\log|\psi_2| - \log|\psi_3|} \tag{19}$$

where ψ_2 is the pressure head for the optimal soil respiration (we assume optimal soil respiration is reached at the saturated soil water content, i.e., $\psi_2 = -0.001$ m), and ψ_3 represents the pressure head when production ceases (we assume a soil water content slightly higher than residual volumetric soil water content $\theta_r = 0.0110$; that is, $\psi_3 = -100{,}000$ m, i.e., $\theta_L = 0.0147$). q_L is the flow rate (m s^{-1}) computed by Eq. (9) (for the unsaturated layer) and Eq. (10) (for the saturated layer below water table). The dispersion coefficient of CO_{2L} (D_L) and the diffusion coefficient of CO_{2G} (D_G) are defined as:

$$D_L = D_{Ls}\tau_L + \lambda_L\left|\frac{q_L}{\theta_L}\right| = D_{Ls}\frac{\theta_L^{\frac{7}{3}}}{\theta_S^2} + \lambda_L\left|\frac{q_L}{\theta_L}\right| \tag{20}$$

$$D_G = D_{Gs}\tau_G = D_{Gs}\frac{\theta_G^{7/3}}{\theta_S^2} \tag{21}$$

where D_{Gs} and D_{Ls} are molecular diffusivity of CO_2 in the gas and dissolved phase, respectively. τ_G and τ_L are tortuosity coefficients for CO_{2G} and CO_{2L} respectively, p is porosity, and λ_L is dispersivity for mechanical dispersion. The mechanical dispersion of CO_{2G} is ignored because gas velocity is too small and the effects of diffusion are generally much greater than dispersion in gas phase (Scanlon et al., 2002).

Concentration of CO_{2L} is related to CO_{2G} by Henry's law constant (K_H), and the CO_2 mass balance equation becomes

$$(\theta_G + K_H RT\theta_L)\frac{\partial CO2_G}{\partial t} = \frac{\partial}{\partial z}D_E\frac{\partial CO2_G}{\partial z} - \frac{\partial}{\partial z}q_E CO2_G + R_G + RC_{CO2} \tag{22}$$

where

$$D_E = \theta_G D_G + K_H RT\theta_L D_L \tag{22a}$$

$$q_E = K_H RTq_L \tag{22b}$$

$$\theta_G = \theta_S - \theta_L \tag{22c}$$

R is the universal gas constant and T is temperature (K).

Transport of Ca^{2+} and other solutes in variably saturated soils. Two processes for Ca^{2+} transport in soil are considered: (1) diffusion and dispersion in water, and (2) transport of dissolved Ca^{2+} (g m^{-3}) by the mass flow of water. The governing equation of mass balance is:

$$\frac{\partial Ca}{\partial t} = \frac{\partial}{\partial z}D\frac{\partial Ca}{\partial z} - \frac{\partial}{\partial z}\frac{q_L}{\theta_L}Ca + RC_{Ca} \tag{23}$$

where $D = D_0\frac{\theta_L^{7/3}}{\theta_S{}^2} + \lambda_{Ca}\left|\frac{q_L}{\theta_L}\right|$, D_0 is the molecular diffusion coefficient for Ca^{2+} in water and λ_{Ca} (m) is dispersivity for mechanical dispersion. RC_{Ca} is the source/sink term (g m^{-3} s^{-1}), representing rate of change in dissolved Ca^{2+} by calcite dissolution/precipitation. Dissolution rate DIS (mmol limestone cm^{-2} s^{-1}) in Eq. (2) can be conveniently converted to RC_{Ca} (g m^{-3} s^{-1}) by

$$RC_{Ca} = \frac{DIS}{dz} \times (40 \times 10^{-3} \times 10^4) \tag{24}$$

with units conversion in parentheses for weathering rate from mmol $CaCO_3$ cm^{-2} s^{-1} to g Ca^{2+} m^{-3} s^{-1}, with calcium molar mass, 40 g mol^{-1}. This can be further converted to weathering rate in the unit of mm calcite per year by the density of solid limestone of about 2.65 g cm^{-3} and an average porosity of 0.37 for limestone in this area (Halley and Schmoker, 1983).

BICY experiences very distinctive dry and wet seasons every year. Soil water content directly influences the precipitation of dissolved calcium and the dissolution of the precipitated calcite in the soil column. Therefore, the model accounts for the chemical reactions occurring in the soil-column by simulating the reactions and transport of all the chemical species relevant for calcite dissolution at different soil layers at each time step:

$$\frac{\partial[H^+]}{\partial t} = \frac{\partial}{\partial z}D_{H^+}\frac{\partial[H^+]}{\partial z} - \frac{\partial}{\partial z}\frac{q_L}{\theta_L}[H^+] + RC_{H^+} \tag{25}$$

$$\frac{\partial[OH^-]}{\partial t} = \frac{\partial}{\partial z}D_{OH^-}\frac{\partial[OH^+]}{\partial z} - \frac{\partial}{\partial z}\frac{q_L}{\theta_L}[OH^+] + RC_{OH^-} \tag{26}$$

$$\frac{\partial[HCO_3^-]}{\partial t} = \frac{\partial}{\partial z}D_{HCO_3^-}\frac{\partial[HCO_3^-]}{\partial z} - \frac{\partial}{\partial z}\frac{q_L}{\theta_L}[HCO_3^-] + RC_{HCO_3^-} \tag{27}$$

$$\frac{\partial[CO_3^{2-}]}{\partial t} = \frac{\partial}{\partial z}D_{CO_3^-}\frac{\partial[CO_3^-]}{\partial z} - \frac{\partial}{\partial z}\frac{q_L}{\theta_L}[CO_3^-] + RC_{CO_3^{2-}} \tag{28}$$

$$\frac{\partial[H_2CO_3^o]}{\partial t} = \frac{\partial}{\partial z}D_{H_2CO_3^o}\frac{\partial[H_2CO_3^o]}{\partial z} - \frac{\partial}{\partial z}\frac{q_L}{\theta_L}[H_2CO_3^o] + RC_{H_2CO_3^o} \tag{29}$$

At each time step in soil, other than the concentration of dissolved CO_2 and Ca^{2+}, the remaining chemical species can be assumed to be in quasi-equilibrium, since the reactions involving these chemical species are fast. The sink/source terms RC's in Eqs. (25)–(29) account for the rates of concentration change for a given chemical species caused by calcite dissolution/reprecipitation.

Boundary conditions for solute transport in variably saturated soils. For the top boundary (soil-air interface), we ignore the convective fluxes of CO_2 and assume that there is a stagnant boundary layer at the soil surface, through which the transport of a gas occurs by vapor diffusion (Simunek and Suarez, 1993), which leads to CO_2 flux at the upper boundary as:

$$J(L,t) = k_{as}(CO2_G(L,t) - CO2_{atm}) \tag{30}$$

where CO_{2atm} is the concentration of CO_2 in the atmosphere (a constant of 400 ppm). k_{as} is the boundary transfer coefficient (m s^{-1}).

For the other solutes, i.e., Ca^{2+}, H^+, OH^-, $CO_3{}^{2-}$, $HCO_3{}^-$, and $H_2CO_3{}^\circ$, at the upper boundary, there is zero flux moving out of the soil-air interface. Using X for the general form of the chemicals, the upper boundary is described as

$$J_X(L,t) = 0 \tag{31}$$

The processes at the lower boundary (soil-bedrock interface) for CO_2 include convective and dispersive flux, and are described as

$$J(0,t) = -D_E\left(\frac{CO2_G(0,t) - GW_{CO2G}}{0.5\Delta z + Z_b}\right)(0,t) + q_E CO2_G(0,t) \tag{32}$$

where Z_b is the distance of bedrock from soil-bedrock interface to the regional groundwater flowpath (with regionally equilibrated solute concentrations) and GW_{CO2G} is the CO_2 in regional groundwater. For the diffusion at the lower boundary, we assume that the chemical composition of groundwater is constant and we use contemporary chemical concentrations of surficial aquifer groundwater in Florida in the model (Lietz, 2000). In the sensitivity analysis, we test how the groundwater chemical concentrations and the choice of Z_b influence weathering rate (details in the section on sensitivity analysis below).

At the lower boundary, fluxes for solutes other than CO_2, i.e., Ca^{2+}, H^+, OH^-, $CO_3{}^{2-}$, $HCO_3{}^-$, and $H_2CO_3{}^\circ$, include diffusion and advection. Using X for the general form, the lower boundary for these chemicals can be summarized as

$$J_X(0,t) = -D_X\left(\frac{X - GW_X}{0.5\Delta z + Z_b}\right)(0,t) + \frac{q_L}{\theta_L}X(0,t) \quad (33)$$

where GW_X is the concentration of X in regional groundwater.

2.2.4. Hydrologic State 2: Soil water dynamics and solute transport in saturated soils

Soil water dynamics in saturated soils. When the wetland soil is the cypress depressions is inundated, the soil is homogeneously saturated. The soil water flux q_L is handled differently between (i) when the water table is below upland soil elevation but still above soil surface in wetland depressions (Fig. 1B) vs. (ii) when the water table is also above upland soil elevation (Fig. 1C). Specifically, when water table is above upland soil elevation, we assume that q_L is constant in time—that is, under the condition of landscape-scale inundation, we assume vertical groundwater loss is largely driven by a constant regional groundwater gradient, as opposed to time-varying head gradient between wetland depression and deeper groundwater. As such, we apply a constant rate of $q_{RGW} = -0.2\,\mathrm{m\,yr^{-1}}$ (Chamberlin et al., *in review*). We later test the sensitivity to a larger range of values. For the case of water table below the surface of upland soil elevation (but above soil surface in depressions) (Fig. 1B), q_L is driven by local head gradient, expressed as

$$q_L = -K_{sat}\frac{h_B - h_A}{z_s} \quad (34)$$

where h_B and h_A are the hydraulic head at point A (at the soil-bedrock interface) and point B (at the soil-surface water interface) (Fig. 1B). We assume that there is no movement of water between subsurface water under upland areas and water below the cypress depressions; that is, point A and point C (at water table of the upland catchment) have the same hydraulic head (Fig. 1B). Therefore, Eq. (34) can be written as

$$q_L = -K_{sat}\frac{h_B - h_C}{z_s} = -K_{sat}\frac{(z_s + \psi_{ws}) - (\Delta L + 0)}{z_s} \quad (35)$$

where z_s is the total soil thickness, ψ_{ws} is the pressure head at point B (equals to depth of surface water; Fig. 1B), and ΔL is the water table in the upland (with bedrock-soil interface as the datum plane). Similar to z_x (in Eq. (10); Fig. 1A), ΔL also features periodic changes in time, driven by evapotranspiration, rainfall, and lateral flow between wetlands adjacent aquifer (similar to McLaughlin et al., 2014). Periodic function with amplitude A_{dL}, period $2\pi/B_{dL}$, and vertical shift C_{dL} could be used to mimic the time variation in ΔL. We varied A_{dL}, B_{dL}, and C_{dL} within meaningful and realistic ranges to test their effects on mean annual weathering rate. Varying the parameter values of A_{dL}, B_{dL}, and C_{dL} could lead to changes in the mean q_L, but model results show that the mean annual weathering rate is controlled by the mean q_L value—the effect of amplitude and frequency is negligible. Therefore, in actual model implementation, we use a constant q_L and later analyze the sensitivity of mean annual weathering rate to the choice of q_L.

We assume that soil is homogeneously saturated, i.e., $\theta_L = \theta_S$ everywhere in soil, as long as the soil is inundated by surface water. Root water uptake (T, $\mathrm{m^3\,m^{-3}\,s^{-1}}$) is included in the model by accounting for its effect on the decline of surface water table. The amount of surface water is determined by several processes: (1) the surface drainage (V_{SD}, $\mathrm{m\,s^{-1}}$), (2) infiltration (k_i, $\mathrm{m\,s^{-1}}$), (3) evaporation (E, $\mathrm{m\,s^{-1}}$) and (4) the total root uptake across the entire soil profile ($\int_0^L T dz$, $\mathrm{m\,s^{-1}}$). The changes in water table (WD, m) can be described as:

$$\frac{\partial WD}{\partial t} = -\left(V_{SD} + k_i + E + \int_0^L T dz\right) \quad (36)$$

When surface water is below spill elevation (ζz_s), $V_{SD} = 0$. Surface drainage occurs when the depth of water on top of soil surface exceeds ζz_s—that is, when the water table is above elevation of a basin's edge and surface water overflows (Fig. S2); in which case, the value of V_{SD} decreases with water depth. V_{SD} can be described by

$$V_{SD}(t) = \begin{cases} 0, & WD \le \zeta z_x \\ \frac{\delta}{e^{(\varepsilon-(WD(t)-\zeta z_s))}}, & WD > \zeta z_s \end{cases} \quad (37)$$

where z_s is total soil depth, and ξz_s describes the elevation distance between upland and the soil surface, i.e., spill elevation. δ and ε are landscape-scale recession rate constants (dimensionless), to adjust how fast the surface drainage rate is when water table is above spill elevation. In the model, we use $\delta = 5 \times 10^{-5}$ and $\varepsilon = 4$, to create an inundation period of ~250 days in a year for a soil column of 1 m (with contemporary precipitation regime in South Florida).

Boundary conditions for the soil water dynamics in saturated soils. Since we assume that the soil is homogeneous vertically, the flux at lower boundary (soil-bedrock interface) is the same as the flux at upper boundary (soil-water interface) and in soil column, and can be expressed as

$$q_L(0,t) = q_L(L,t) = \begin{cases} -K_{sat}\frac{z_s + \psi_{ws} - \Delta L}{z_s}, & z_s + \psi_{ws} \ne \Delta L \\ q_{RGW}, & z_s + \psi_{ws} = \Delta L \end{cases} \quad (38)$$

Transport of solutes in saturated soils. In saturated soils, we considered two processes for the transport of CO_{2L}: diffusion and advection. Transport of CO_{2G} in saturated soils is negligible. The mass balance equation for CO_2 in saturated soil is:

$$\frac{\partial CO2_L\theta_L}{\partial t} = \frac{\partial}{\partial z}\left(\theta_L D_L\frac{\partial CO2_L}{\partial z} - q_L CO2_L\right) + R_G + RC_{CO2} \quad (39)$$

where R_G is the production of CO_2 by soil respiration and is calculated in the same way as R_G in unsaturated soils described previously (Appendix C), except that in saturated soils, we assume that roots (and thus respiration) do not experience water stress ($f_s = 1$ in Eq. (19)). The transport of Ca^{2+} and the remaining solutes (H^+, OH^-, HCO_3^-, CO_3^{2-}, and $H_2CO_3^*$) are modeled similarly as in variably saturated soil (Eq. (23), Eqs. (25)–(29)).

Boundary conditions for solute transport in saturated soils. Soils are inundated by a layer of sheet flow (or standing water) during the wet season of BICY. CO_2 exchange at the soil-water interface, J_{ws} ($\mathrm{mol\,m^{-2}\,s^{-1}}$), includes diffusion of CO_{2L} between soil and overland flow and infiltration-mediated flux into soil. J_{ws} is described by

$$J_{ws}(t) = k_L(CO_{2L}(0,t) - CO_{2LW}(t)) + k_i CO_{2LW}(t) \quad (40)$$

where CO_{2LW} is the average concentration of CO_{2L} in overland flow. We assume an instantaneous complete mixing of solutes in overland flow (Dong and Wang, 2013). k_L ($\mathrm{m\,s^{-1}}$) is the mass transfer coefficient between the soil upper boundary and overland flow. k_i ($\mathrm{m\,s^{-1}}$) is the infiltration rate. The concentration gradient at the water-air boundary is created by the difference between CO_{2L} in water and CO_{2L} in equilibrium with the partial pressure of atmospheric CO_2, P_{CO2}. The air-water flux J_{wa} ($\mathrm{mol\,m^{-2}\,s^{-1}}$) is defined as

$$J_{wa}(t) = k_{La}(CO2_{LW}(t) - K_H P_{CO2}) \quad (41)$$

where k_{La} is the gas CO_2 transfer rate at the water-air boundary.

The flux of CO_2 by surface drainage is

$$J_{SD}(t) = CO2_{LW}(t)V_{SD}(t) - CO2_{in}V_{SD}(t) \quad (42)$$

where CO_{2in} is the concentration of CO_{2L} in water from upstream. Taking into consideration the effect of water-soil exchanges, water-air exchanges, surface drainage, infiltration, and evaporation, CO_{2L} in overland flow is

$$CO2_{LW}(t+1) = \frac{CO2_{LW}(t)WD(t) + (J_{ws}(t) - J_{wa}(t) - J_{SD}(t))dt}{WD(t) - (-k_i + E)dt} \quad (43)$$

For other chemicals species that do not have a gas phase, i.e., Ca^{2+}, H^+, OH^-, HCO_3^-, CO_3^{2-}, and $H_2CO_3^*$, the flux at the upper boundary (soil-water interface) is expressed as

$$J_{ws,X}(t) = -D_L\left(\frac{\partial X}{\partial z}\right)(L,t) = k_L(X(0,t) - X(t)) + k_i X(t) \quad (44)$$

where X is the concentration of the dissolved chemical species X in overland flow water, and k_L is the mass transfer coefficient. The flux of solute by surface drainage is

$$J_{SD,X}(t) = X(t)V_{SD}(t) - X_{in}V_{SD}(t) \quad (45)$$

where X_{in} is the concentration of X from upstream flow. The concentration of X in overland flow is expressed as

$$X(t+1) = \frac{X(t)WD(t) + (J_{ws,X}(t) - J_{SD,X}(t))dt}{WD(t) - (-k_i + E)dt} \quad (46)$$

The lower boundary for CO_2, Ca^{2+}, H^+, OH^-, HCO_3^-, CO_3^{2-}, and $H_2CO_3^\circ$ is addressed in the same way as in unsaturated soil (Eq. (33)).

2.2.5. Model initial conditions

The initial hydrological condition of the model is homogeneously saturated soil, with a thin layer of standing water (0.005 m), i.e.,

$$\theta_L(z,0) = \theta_s \quad (47)$$

CO_2 concentration in equilibrium with atmospheric CO_2 is used as the initial CO_{2L} in soil. The initial condition for Ca^{2+} is set to zero. The initial concentrations of H^+, OH^-, CO_3^{2-}, HCO_3^- and $H_2CO_3^\circ$ are solved under the assumption of chemical equilibrium with given CO_2 and Ca^{2+} concentrations. The models are run for 1.5 yrs. of model time (initiated in April of the preceding water year), to eliminate the effect of initial conditions. Weathering rate is represented by mean annual weathering rate, discarding the first six-month burning-in period.

2.2.6. Model implementation and evaluation

The set of differential equations for soil water and solute transport was solved with the finite difference method with appropriate time steps and spatial resolution that satisfy the Courant-Friedrich-Lewy condition, for a desired calculation accuracy and numerical stability. Vertical spatial resolution was 2 cm. The model uses two time steps: an outer time step during which transport processes are calculated (Δt_{outer} = 10 s), and an inner time step (Δt_{inner} = 0.1 s) nested within the outer time step that is used to solve for chemical reactions. For soil water retention, we used the mixed form of the Richard equation to maintain mass conservation. We combined a finite difference approximation of the mixed-form equation with a modified Picard iteration scheme (a fully implicit time approximation) (Celia et al., 1990), and used the convergence criterion proposed by Huang et al. (1996) for computation efficiency. We compared the modeled CO_{2L} and Ca^{2+} profile in soils with the observed data (method of data collection described in Appendix D) under the corresponding hydrological state, to evaluate model performance.

2.3. Controls of weathering rates (sensitivity analysis)

We carried out both local and global sensitivity analysis with a host of variables in the model. Local sensitivity analysis is one-factor-at-a-time approach: we examined the sensitivity of weathering rate to each variable, while holding the values of remaining parameters at values typical for BICY (Table S1). Results from local sensitivity analysis indicate how each parameter influences weathering rate within the parameter space of our focal study system. We then used the Morris global sensitivity analysis method (Morris, 1991) for simultaneously—instead of one factor at a time—testing the sensitivity of the same list of parameters examined in local sensitivity analysis (listed in Table S2). The Morris method is designed for complex (e.g., nonlinear effect by parameters, interactions among parameters) and computationally intense models. In addition to ranking the relative first-order importance of each factor on the model output, this method measures second- and higher-order effects in which the factor is involved: nonlinear effects and/or interactions with other factors (Saltelli et al., 2004; a detailed description of Morris method is provided in Appendix E). For global sensitivity, we analyzed the sensitivity of 11 parameters (processes) of interest (listed in Table S2).

2.4. Soil thickness feedbacks on weathering rate

We explored how the mean annual weathering rate changes with the thickening of soil cover on bedrock: potential responses include linear increases, linear decreases, or nonlinear responses. Furthermore, we investigated whether and how the magnitude of rates and the shape of this relationship changes with environmental conditions.

2.5. Estimating fluxes and mass balance

We estimated the carbon and calcium mass balance at the scale of an individual cypress depression. We ran the model for six evenly-spaced sites along a transect extending from the center of a basin to the edge (Fig. S2). For points from the center to the edge, soil cover, biomass, threshold water depth (above which surface drainage occurs), and inundation period decrease. For the sites located on the edge, surface drainage occurs as long as there is surface water. For the sites in the center, once the water depth is below the elevation of the upland, surface drainage stops (i.e., the basin is isolated). We kept track of various fluxes of carbon and calcium and derived the mass balance for each point. Finally, we scaled up the results at each point to estimate mass balance of carbon and calcium at the scale of individual depressions (more details on estimating mass balance is provided in Appendix F).

2.6. Estimating age of cypress depressions

We estimated the age of wetland depressions as the time required to weather 2 m of limestone, i.e., a typical bedrock depth in the center of cypress domes in present-day BICY. We assume no variation in climatic conditions (e.g., precipitation, temperature, regional groundwater chemical status; the effect of this assumption is explored later in the paper) over the period of landscape development, and the change in weathering rate is only driven by the thickening of soil cover on bedrock. The soil cover (consists of insoluble weathering residuals and accumulation of organic matter) on bedrock is assumed to be a linear function of bedrock depth, with a coefficient of 0.65 (Watts et al., 2014). We then parameterize the model with values describing conditions in BICY (Table S1), and compute the mean annual weathering rate for soil thickness of 0 cm (i.e., bedrock depth = 0 m, exposed), 6.5 cm (i.e., bedrock depth = 0.1 m), 13 cm (bedrock depth = 0.2 m), 19.5 cm (bedrock depth = 0.3 m), …, 123.5 cm (bedrock depth = 1.9 m), and 130 cm (bedrock depth = 2 m). The weathering rate at other soil thicknesses is linearly extrapolated from the rates computed. The time it takes to weather 2 m limestone is expressed as

$$age = \sum_{n=1}^{20} \int_{z_1=0.1(n-1)}^{z_2=0.1n} \frac{1}{R_w(z)}dz = \sum_{n=1}^{20} \frac{1}{a}(\ln(\alpha z_2 + \beta) - \ln(\alpha z_1 + \beta)) \quad (48)$$

where z_1 and z_2 is interval of 10 cm from 0 to 2 m, $R_w(z)$ is the mean annual weathering rate (m calcite yr^{-1}) at bedrock depth z (i.e., soil cover = 0.65z; $z_1 \le z \le z_2$). α and β are

$$\alpha = \frac{R_w(0.1n) - R_w(0.1(n-1))}{0.1n - 0.1(n-1)} \quad (48a)$$

$$\beta = R_w(0.1(n-1)) - 0.1(n-1) \times \frac{(R_w(0.1n) - R_w(0.1(n-1)))}{0.1n - 0.1(n-1)} \quad (48b)$$

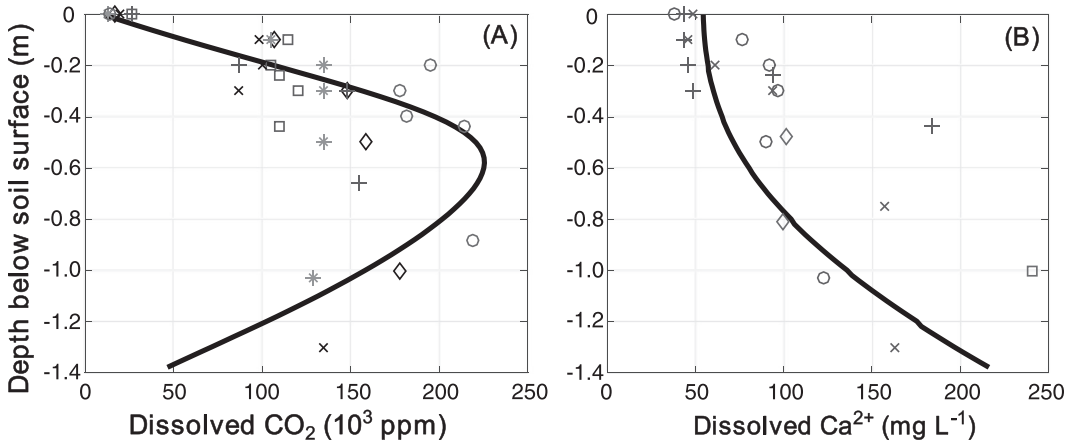

Fig. 2. Comparison of modeled (solid line) and observed soil profiles of (A) dissolved CO_2 and (B) dissolved calcium in soil column. Different symbols represents data collected from different sites or different locations within same sites (see Appendix E for field data collection). Model parameters were not fit to data.

3. Results

3.1. Evaluating model performance

We assessed the performance of the model with empirical data from BICY by comparing aggregated profiles of dissolved CO_2 and Ca^{2+} from field measurements. Both the shape of the profile and the range of values had a reasonable goodness-of-fit between modeled and measured results (Fig. 2): for CO_2 profile, the Nash-Sutcliffe model efficiency coefficient (identical to the coefficient of determination, R^2, in their formula, but typically used in simulation models; Moriasi et al., 2007) is 0.43, and for Ca^{2+}, it is 0.37.

3.2. Controls on weathering rate

3.2.1. Local sensitivity analysis

For sensitivity under local conditions (i.e., where the value of one factor at a time is changed, while other parameters are fixed to the parameter space describing the condition of BICY), weathering rate was most sensitive to biological characteristics (total biomass and vertical distribution of root biomass; see heat ramps in Fig. 3G–H), followed by processes influencing hydrology (annual rainfall, monthly rainfall distribution, and spill elevation; Fig. 3A–D), and transport rate (groundwater drainage, dispersion/diffusion; Fig. 3E–F). The effect of chemical status at upper and lower boundaries (chemical concentrations in overland flow and in the regional groundwater; Fig. 3I–J) on weathering rate was negligible.

Biological characteristics – With no biogenic acid, weathering rate was about 9.5 mm kyr^{-1} but increased sharply with soil respiration (Fig. 3G). In BICY, the weathering rate was estimated to be 190 mm kyr^{-1} (1 m soil cover), about 20 times higher than that with no biogenic CO_2. Among all the variables examined in this study, the morphology of the root system was most critical (Fig. 3H). At equal amounts of root biomass, when a greater proportion of root mass was distributed in the upper soil layers, more CO_2 left the system to atmosphere as gas emission than moved downwards to bedrock to enhance chemical weathering (Fig. S3-F). Hence, shallow roots led to reduced weathering rate.

Hydrology – Both the amount of annual rainfall and its temporal distribution in a year (Figs. S4, S5) affected weathering rate (Fig. 3A–D). Weathering rate first linearly increased with annual rainfall, and then leveled off (at $\sim$ 1.4 m yr^{-1}) with further increase in annual rainfall (Fig. 3A). Holding annual precipitation constant, weathering rate was enhanced under a more clustered rainfall regime, compared to the regime where rainfall was more evenly distributed throughout a year (Fig. 3B). However, with more rapid surface runoff (e.g., steeper landscapes, hillslopes) than occurs in Big Cypress, this pattern would be reversed: a more uniform rainfall distribution produced higher weathering rates (Fig. 3C). With fixed amount of annual precipitation, higher spill elevation—the elevation above which rapid declines of water tables occurs—enhanced weathering rate (Fig. 3D).

Rate of transport – In general, increases in material transport rate enhanced weathering (Fig. 3D–F). Systems with zero groundwater drainage (i.e., advective flux = 0) had a very slow weathering rate, whereas a small increase in groundwater drainage (from 0 to 5 cm yr^{-1}) led to a dramatic increase in weathering rate (Fig. 3E). Still further increases in groundwater drainage (beyond 20 cm yr^{-1}) generated a minor decline in weathering, where rapid groundwater drainage shortened the period of landscape inundation.

Chemical concentrations in groundwater and overland flow – We investigated the effect of chemical status (concentration of various solutes in saturated water with respect to calcium) of the upper and lower boundaries on bedrock weathering. At both boundaries, as the concentrations of dissolved CO_2 and Ca^{2+} increased (all in saturation state with respect to calcium), weathering rate decreased (Fig. 3I–J). The sensitivity of weathering rate to the chemical concentrations of groundwater and overland flow was low, however. With tripling in saturated Ca^{2+} concentration in groundwater, weathering rate declined by only 20% (Fig. 3I). The effect of CO_2 in overland flow was negligible (Fig. 3J).

3.2.2. Global sensitivity analysis

The global sensitivity analysis is designed to account for the complex interactions among parameters and their potential nonlinear effects in the model. Weathering rate was most sensitive to annual rainfall and thickness of soil cover, followed by total root mass (linearly correlated to soil respiration) and its vertical distribution in soil (Fig. 4). We classified these variables as first-order controls on weathering rate due to their large effect on the rate of weathering. Following in importance were distance between weathering front and regional groundwater table, dispersion rate, drainage rate of groundwater and its chemical status, runoff rate, and rainfall regime, all of which were considered of secondary importance (Fig. 4). Chemical status of overland flow had a negligible effect. Of all variables, total root mass had the highest interaction effect, i.e., its effect size was highly contingent on the position of the system in the parameter space of the remaining variables (as indicated by the high σ value in Fig. 4). Following root mass, annual rainfall, thickness of soil cover, and vertical distribution of root mass had strong interaction effects (Fig. 4).

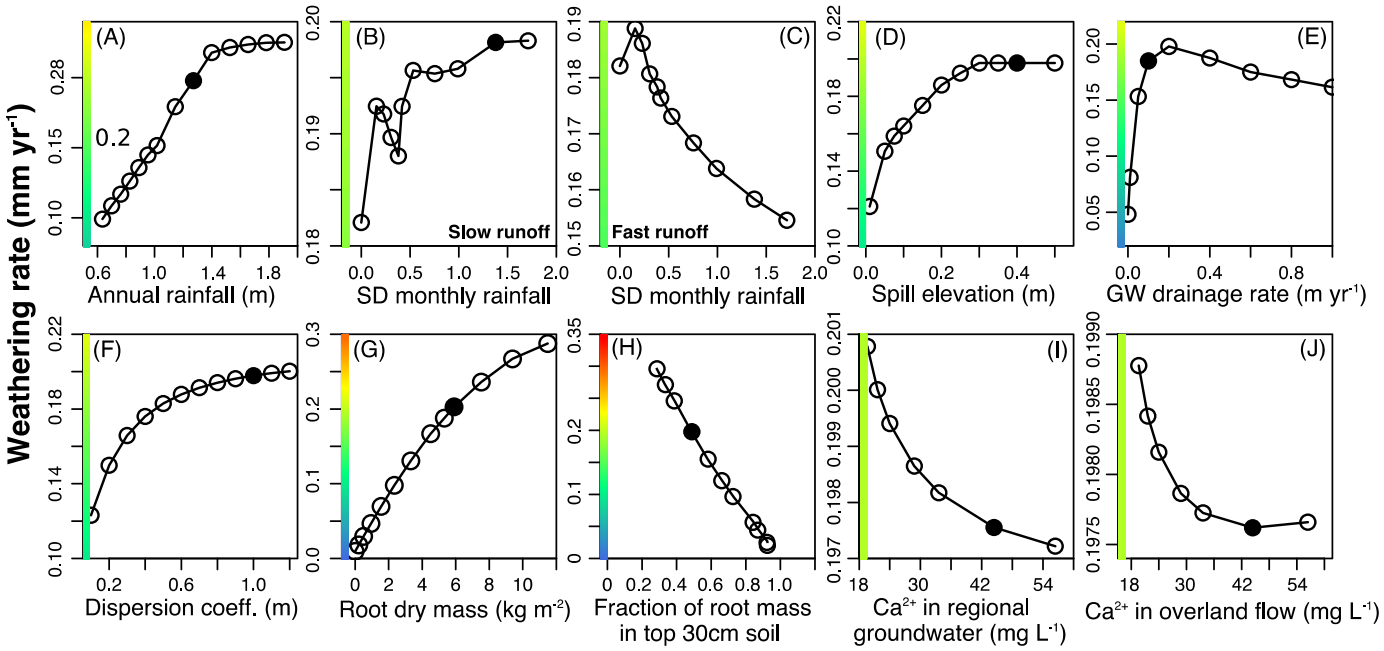

Fig. 3. Effect of ten variables on limestone weathering rates (with all others parameterized for Big Cypress National Preserve). The heat ramp in each plot emphasizes the range of each y-axis range in comparison with other variables. The solid dots represent the parameter value most appropriate for Big Cypress (no solid dot in C, since the case in BICY is slow runoff in B). "SD monthly rainfall" in (B) and (C) refers to the standard deviation of monthly rainfall depth in a year; "Spill elevation" in (D) refers to the threshold water table above which water table exceeds the elevation of upland and surface drainage occurs. "Dispersion coeff." in (F) refers to the parameter dispersivity used to calculate dispersion: a greater value of dispersion coefficient implies a greater dispersion rate.

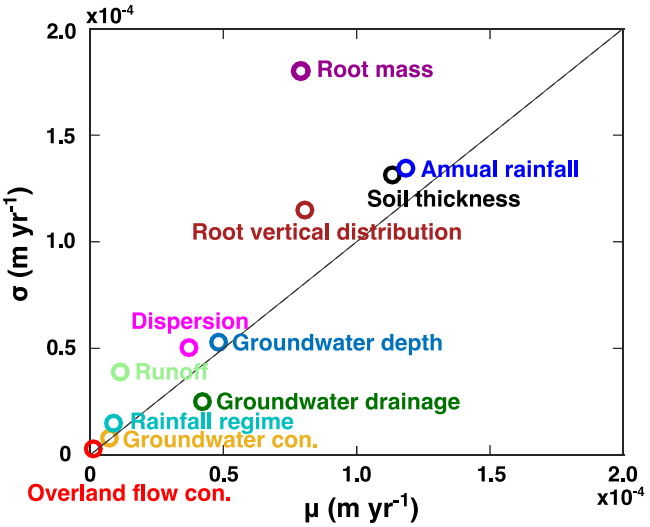

Fig. 4. Global sensitivity analysis of 11 variables in the model; *x*-axis denotes the mean effect of the factor, and *y*-axis is the standard deviation of the factor on the output variable (rate of chemical weathering) evaluated at 16 independent positions in the parameter space. 'Rainfall regime' refers to the variability of monthly rainfall in a year.

3.3. Feedback between soil thickness and bedrock weathering

To determine whether weathering rate increases or declines with thickness of soil cover and how environmental conditions regulate this relationship, we varied soil thickness under: (1) three levels of groundwater drainage rate; (2) three levels of annual rainfall; (3) three different rainfall regimes under two levels of surface runoff rate, and (4) three vertical distributions of root biomass.

Overall, a maximum in weathering rate occurs that depends on soil thickness (Figs. 5 and S6). However, —the soil thickness where the rate was maximized (Z_{max}) varied with environmental variables. When the system featured high groundwater drainage, abundant rainfall, and/or deep roots, the negative effect of additional soil cover did not appear until soil cover was at least 1.6 m (Fig. 5-A1, D1, E1). On the contrary, if groundwater drainage was low, climate was dry, and the root system was shallow, this negative relationship could occur when soil cover was only 0.2 m (Fig. 5-E3), lower than in dry climate with shallow roots. In systems with very shallow roots, the negative relationship started at soil thickness = 0 because limited CO_2 could reach bedrock. With soil thickening, weathering rate increased again as produced CO_2 reached bedrock (Fig. 5-E3). Equilibrium CO_2 concentrations at bedrock surface are reached for all soil thickness in a short period of time. After that, bedrock weathering becomes limited by export of weathering products. Deeper soils have greater mean advective flow rate (everything else being equal), hence, the weathering kinetics are less limited by export of weathering products.

The effect of rainfall regime on Z_{max} depends on the rate of surface runoff. When surface runoff is low (as in BICY), more clustered rainfall (i.e., distinctive dry and wet seasons) resulted in a greater threshold soil thickness, i.e., the negative effect of soil thickness on weathering rate did not begin until the soil cover on bedrock was around 1.6 m thick (Fig. 5B). In contrast, when surface runoff was rapid, more uniform rainfall distribution resulted in a greater threshold soil cover (Fig. 5C).

3.4. Fluxes and mass balance in BICY

With thickening of soil cover, the ratio of export via upper boundary (to atmosphere and/or to surface drainage) to export via lower boundary (to groundwater) changed for both calcium and carbon (Fig. 6). For calcium, this ratio (export via upper boundary to via lower boundary) decreased with soil depth—approximately two orders of magnitude reduction as soil cover increases from 30 cm to 180 cm (Fig. 6A). In contrast, a greater proportion of CO_2 left via the upper boundary as soil thickened, and the increases in the proportions steepened after ~140 cm soil thickness (Fig. 6B). Additionally, the fraction of CO_2 from respiration consumed by bedrock weathering decreased linearly as soil cover thickens, from about 35% with 10 cm soil cover

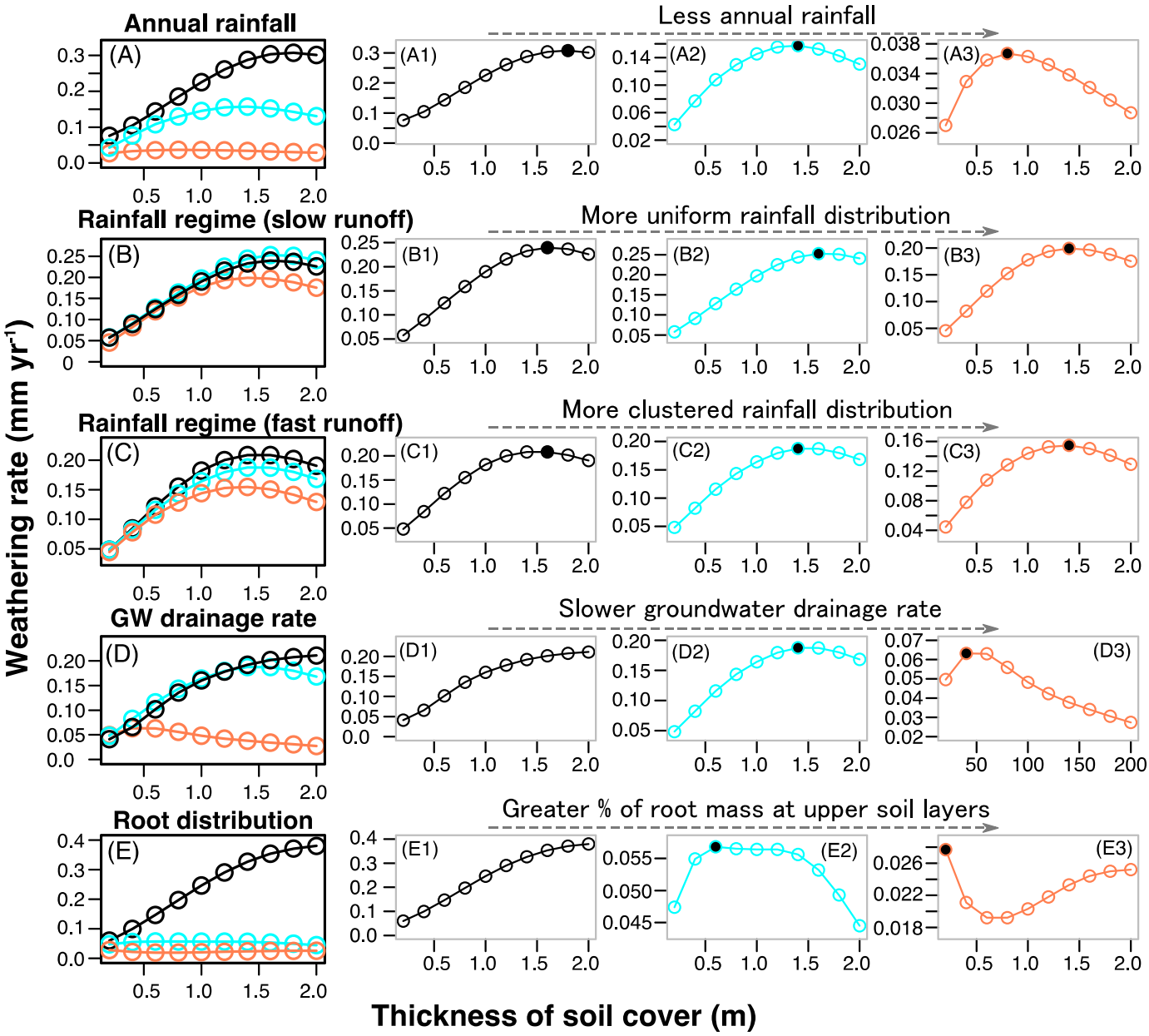

Fig. 5. Weathering rates as a function of soil cover thickness influenced by (A) total amount of annual rainfall, (B) rainfall regime (under low surface runoff rate), (C) rainfall regime (under high surface runoff rate), (D) groundwater drainage rate, and (E) morphology of root system (the vertical distribution root mass in soils). The effect of each variable was assessed at three levels: three levels were plotted together in column 1, and each level was then plot separately in columns 2–4 with rescaled *y*-axis to show the soil thickness where maximum weathering rate is reached (black solid points).

to < 5% with 180 cm soil cover (Fig. S7). Lastly, for both calcium and carbon, the ratio of export via upper boundary and export via lower boundary was influenced by a range of variables (e.g., groundwater drainage, runoff, annual rainfall etc. Figs. S3, S8, S9).

Integrating six points along a transect from the center to the edge of a basin, we estimated calcium and carbon mass balance at a basin scale. For the point on the edge, almost all dissolved Ca^{2+} was exported via surface flow (14.3 g Ca^{2+} $m^{-2}y^{-1}$); for the point in the center of a dome, two thirds of weathered Ca^{2+} left via groundwater (55.4 g Ca^{2+} $m^{-2}y^{-1}$), and the remaining one third (27.0 g Ca^{2+} $m^{-2}y^{-1}$) was exported via surface flow. For carbon, the groundwater exports were 4.4 g C $m^{-2}yr^{-1}$ and 0.04 g C $m^{-2}yr^{-1}$ for the sites at the center and the site on the edge; the surface export were 41.8 g C $m^{-2}yr^{-1}$ and 2.3 g C $m^{-2}yr^{-1}$ at the center of the basin and on the edge, respectively. Scaling up these site-level estimates, at a basin scale (conical shape; 50 m in radius and 2 m in depth; Appendix F), we estimate that about 8.3×10^4 g Ca^{2+} left the basin via groundwater and 1.7×10^5 g Ca^{2+} left via surface flow (Table S3). This value suggests export via surface drainage as the major Ca^{2+} outlet—twice that via groundwater. For carbon, about 4.9×10^3 g carbon left the basin via groundwater and 4.3×10^4 g carbon left the basin via soil surface (Table S3). Averaging over the entire basin, about 29% of the CO_2 produced by biological respiration was consumed in for bedrock weathering (Table S3). The remaining 71% of CO_2 left the soil column via the lower and upper boundary, of which 90% left via upper boundary as gas emission. However, these results vary with the treatment of diffusion length at the lower boundary (Table S4).

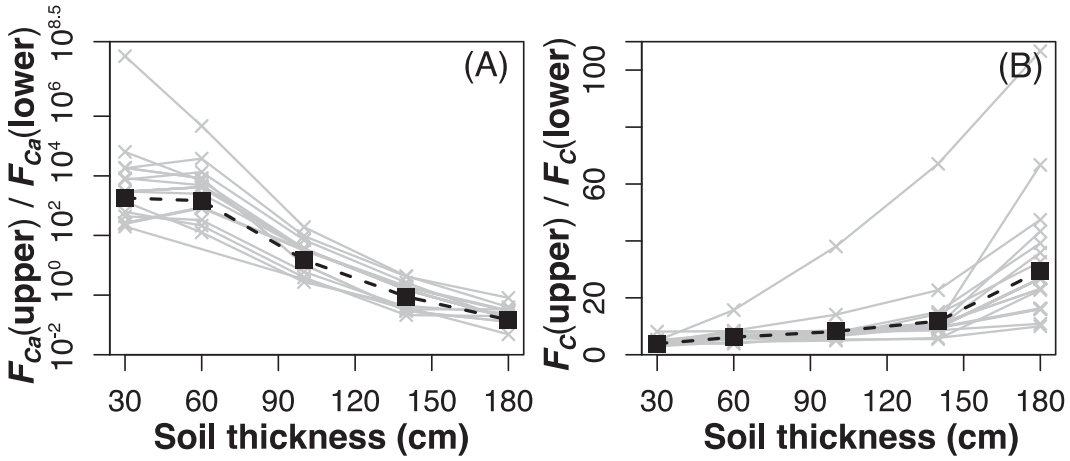

Fig. 6. Fluxes of calcium and carbon export as a function of the thickness of soil cover. (A): the ratio of dissolved calcium export via surface drainage (upper boundary) and via groundwater drainage (lower boundary); and (B): the ratio of carbon export via surface drainage and gas emission (upper boundary) and via groundwater drainage (lower boundary). The grays 'x' symbols represent results from model runs with different parameter values (runoff rate, groundwater concentration, groundwater drainage rate, rainfall regime, dispersion rate, amount of annual rainfall, and root vertical distribution); and the solid black squares denote the mean of the values for the corresponding soil thickness across all parameter values examined.

3.5. Age of cypress depressions

Using parameters specific to BICY (Table S1), we estimated the age the landscape development by soil thickness-specific weathering rates (Eq. (48)). The model estimated that the wetland depressions in BICY are about 9478 yrs. old. That is, ~9500 simulated years are needed to weather 2 m of limestone bedrock, the typical bedrock depth in the center of domes on the landscape (Watts et al., 2014).

4. Discussion

Chemical weathering of bedrock is not only controlled directly by an array of climatic and geologic variables, it is further complicated by interactions and feedbacks among environmental variables, local ecohydrologic processes, and the internal feedback between soil thickness and weathering rate (Fig. 7). Here using the limestone landscape of Big Cypress National Preserve in South Florida as a case study, we develop a reactive-transport kinetics model to investigate the formation and control of the limestone depressions in this system. The results of this model concur with observed vertical distributions of Ca^{2+} and CO_2, and with several independent estimates of the vertical rate of depression expansion, suggesting that the model captures the most important processes controlling limestone bedrock weathering over both short and long time scales. The flexibility of the model allows us to make broader inferences about the relative importance of environmental controls, the strength of interactions among these environmental variables, and the mediating and amplifying effects of local ecohydrologic processes and internal feedbacks.

4.1. Landscape evolution in Big Cypress

Model simulations suggest that Big Cypress National Preserve wetland depressions started to develop around 9.5 kyrs ago, near the end of the Last Glacial Maximum (11.7–13.0 kyrs B.P.) and the beginning of the Holocene (10 kyrs B.P.). This model estimate is comparable to the 7 kyrs B.P. (95% confidence interval of 3043–19,297 yrs) estimated from landscape-scale mass balance of Ca and P, which is based on modern Ca and P accumulation and export, without accounting for historic changes in weathering rate (Chamberlin et al., *in review*).

Considering the bias embedded in several modeling assumptions, it is likely that wetland depressions in BICY started to develop later, rather than earlier, than our model-derived estimates (i.e., younger than

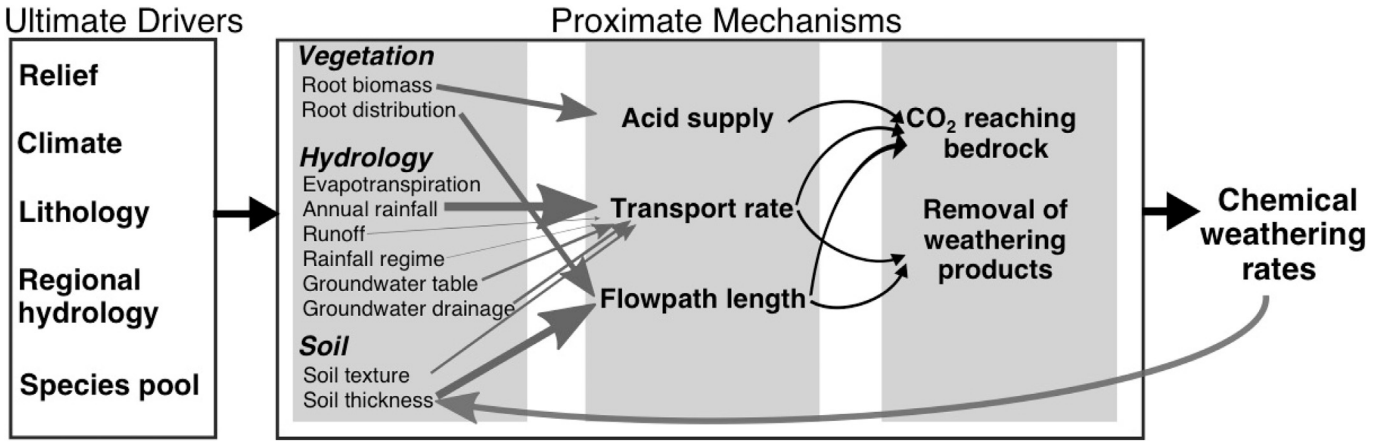

Fig. 7. Ultimate and proximate drivers influencing limestone weathering through their effects on flowpath length (between source of acid and reaction site), transport rate, and acid supply, all of which eventually influence both the amount of CO_2 reaching the bedrock surface and removal of weathering products from reaction sites to affect rate of chemical weathering. The thickness of the gray-colored arrows (between the first and second gay box and feedback from 'chemical weathering rates' to the first gray box) is proportional to their effect size on rate of chemical weathering in our reactive transport model.

9.5 kyrs). In the model, we made a simple assumption of a linear relationship between root biomass and soil cover (Appendix C); however, vegetation that is currently and historically abundant in BICY uplands (i.e., pines) can exploit thin, nutrient poor soils, and even grow in joints in rock outcrops. Pollen records show the dominance of *Pinus* spp. (pine) in the pre-Holocene in BICY (Watts and Hansen, 1994). Therefore, it is likely that the weathering rate at the initial stage of forming these depressions was greater than the model predicted. Moreover, pre-existing bedrock porosity and overlying marine sediments likely favored deeper and more persistent moisture during early weathering stages than our simplifying assumptions reflect. In the model, with the very slow weathering rate at the initial stages, it takes ~4100 yrs. to dissolve the first 20 cm of bedrock. Additionally, we only considered the effect of inorganic acid (CO_2) produced by plants, without taking into consideration other forms of acids (e.g., organic acid), which have been shown to enhance chemical weathering (Drever and Stillings, 1997). Given the parameter values describing BICY, the model predicts a slowing of weathering rates after reaching a critical soil cover of about 1.5 m (Fig. 5). This implies that the deepest portions of the landscape are close to maximum weathering rate currently, and the rate is starting to slow due to the negative feedback between soil cover and weathering rate.

One of the biggest uncertainties in long-term estimates of weathering rate involves past variations in climate and associated biological activities, especially because precipitation and biological characteristics are both first-order variable controls on weathering rate (Fig. 4). Sediment pollen records show that at about 10 kyrs B.P., oak and pine dominated with grasses and other herbs in BICY, as a response to ongoing aridity (Watts and Hansen, 1994). In the mid-Holocene between ≈7 and 5 kyrs B.P., there is a well-studied increase in wetness caused by intensification of the El Niño-Southern Oscillation (ENSO), which increased the winter precipitation and lengthened annual hydro-period in Florida (Donders et al., 2005). The intensity of surface sheet-flow across the landscape significantly affects weathering rate (Fig. 3). Meanwhile, cypress trees became steadily more abundant over time, until they became the dominant pollen type, as sea level continued to rise and much flooding of shallow basins took place (Watts and Hansen, 1994; Ross et al., 1994; Donders et al., 2005). Cypress trees in general have deeper roots than pines: about 25–30% of root biomass is below the first 30 cm soil layers. For pines it is about 10% (Montague and Day, 1980). Such a change in vertical distribution of root mass as a consequence of shift in vegetation type would also enhance weathering, because root morphology is a first-order control (Fig. 4).

4.2. Controls on weathering rate

We developed a model framework to not only investigate the specific weathering process in BICY, but also to make broader quantitative inferences about the relative importance of a wide range of environmental variables on weathering rate, through their effects on acid supply, path length (distance between source of acid and bedrock), and vertical transport, all of which ultimately control the amount of CO_2 arriving at bedrock to participate in weathering (Fig. 6). The most general conclusion of our analysis is that climate, soil structure, and biotic activity are approximately co-equal in their importance for limestone weathering. Moreover, higher-order and interactive effects of these variables are as important as first order effects, meaning that the effects of individual variables are likely to be context-dependent. As a result, linear extrapolation of weathering rates from one setting to another based on effects of single variables is likely to be erroneous, and we should not expect any specific individual variable to effectively predict weathering rates across physiographic and ecological settings.

Our model provides a quantitative tool to understand the varied effects of biogenic CO_2 in conjunction with the many other geophysical and ecohydrologic processes that affect weathering. The effect of biogenic CO_2 on the dissolution of limestone has been extensively reported (e.g., Murray and Love, 1929; Woo and Marsh, 1976; Hinsinger et al., 2001), and biotic enhancement of weathering ranges from a factor between 1 and ~20 (Drever, 1994; Moulton and Berner, 1998; Moulton et al., 2000; Lucas, 2001; Hinsinger et al., 2001). For systems similar to BICY in their climate, vegetation, and lithology, we estimated an acceleration of ~20 fold by soil respiration, at the high end of the range of values reported in the literature and consistent with other values reported in this region (Gulley et al., 2015). The high value could be attributed to the long inundation period in BICY, which resulted in high retention capacity of soil CO_2 produced by high vegetation biomass in the wetland depressions (Fig. S9-E). Additionally, the region's bedrock limestone has high reactivity and may favor stronger effects of biogenic acidity.

CO_2, once produced by respiration in the upper soil zone, must be transported through the soil column to the bedrock surface for weathering; that is, the net chemical effect of plants on weathering is not only determined by the amount of CO_2 produced, but also by transport processes in soil (Fig. 6). Rate of transport is closely related to the hydrologic state of soil, and hydrology is often considered to affect weathering rate via influencing fluid flow rates and residence times (Maher, 2010). Our results indicate that the inhibition of atmospheric gas exchange under inundated conditions is an additional important mechanism by which hydrology affects weathering rate. Conditions such as high rainfall and/or low runoff that favor longer inundation and higher soil water content enhance weathering (Fig. 3A–D). With the same annual precipitation, interplay between runoff and rainfall temporal distributions determines water residence time: with rapid runoff (e.g., hillslope), more evenly distributed rainfall maintains higher mean soil water content (Fig. 3C). With slower runoff (e.g., in low- relief systems like BICY), a more clustered precipitation regime likely results in higher water retention (Fig. 3B). Landscape relief not only affects surface runoff, but also sub-surface drainage, both of which control water retention in the system, and therefore transport rate and weathering. Prolonged hydrological inundation, however, changes redox conditions, which inhibits biological respiration, and hence reduces acid production for weathering. In BICY specifically, baldcypress (*Taxodium distichum*) uses cypress knees to allow easy diffusion of O_2 from the atmosphere to submerged root zone (Martin and Francke, 2015). In a more general case, if the model took into consideration the negative effect of inundation on CO_2 production, we would expect a less pronounced positive effect of hydroperiod on limestone weathering rates.

The effects of transport rate on bedrock weathering are important, but complex. Some factors that favor rapid delivery of reactants to the weathering front also favor water loss (Fig. 3E). Rapid transport in the vertical dimension (i.e., groundwater drainage) could enhance weathering at the bedrock surface (Fig. 3); however, high transport rate reduces the contact time between water-mineral interactions along subsurface flowpaths in the lateral dimension (i.e., hillslope), which has been demonstrated to reduce weathering rate (Gabet et al., 2006; Maher and Chamberlain, 2014). Rapid drainage also reduces the duration of inundation. Whether the net effect of rapid transport is positive or negative depends on the rate-limiting mechanisms (Berner, 1978; Maher, 2010). In natural systems, transport-limited weathering is ubiquitous (Kump et al., 2000; Maher, 2010).

Transport limitation can be evaluated by comparing the mean travel time to the time required to reach chemical equilibrium (i.e., Damoköhler number; Boucher and Alves, 1959). Chemical weathering of silicate rocks, with lower reactivity, would likely be more sensitive to the transport in the lateral dimension (seepage velocity), with reaction approaching equilibrium along the flowpath of a hillslope (Gabet et al., 2006; Maher and Chamberlain, 2014). Consequently, in silicate terrains, slower transport rates, and hence longer residence times, would enhance weathering rate. In contrast, calcite weathering has faster kinetics and greater solubility than most silicate rocks (Liu et al., 2011). Thus, reaction limitation is likely more common in calcite weathering.

This relative difference in reaction rates suggests that acid supply by vertical transport may play a greater role in calcite than silicate weathering and a rapid vertical transport rate increases weathering of calcite. We assumed homogeneous soil structure with no preferential flow paths in soils, which likely have underestimated the transport of biogenic acid to bedrock surface, hence, understating weathering rate (Gerke, 2006). A better estimation of chemical weathering rates requires accounting for a heterogeneous soil structure with more realistic structured porosity and transport of water and solute.

Weathering of carbonate rocks has often not been thought to be an important mechanism that sequesters CO_2 over geologic time scales, because all of the CO_2 consumed in the weathering process is returned to the atmosphere by the comparatively rapid precipitation of carbonates in the oceans (Berner et al., 1983; Elderfield, 2010). However, recent studies with new techniques suggest a significant underestimation of the importance of carbonate weathering as an atmospheric CO_2 sink (Jacobson et al., 2002; Quade et al., 2003; Liu et al., 2011). Models like the one in this study could be expanded in future studies to understand the controls of carbonate weathering at broader spatial scales to better understand atmospheric CO_2 and bedrock weathering feedbacks over geological time.

Thickness of soil cover on bedrock is intimately related to both biogenic CO_2 source and the transport processes discussed above (Carson and Kirkby, 1972; Ahnert, 1988). Thin soils can support a limited amount of biological activity and hold little water. Thicker soils support more biological activity, hence more respirational CO_2 and enhanced weathering. However, with soil thickening, the longer path length between bedrock and acid source eventually limits weathering. The maxima shown in the relationship between the thickness of overlying soil and weathering indicates that weathering first increases with soil cover, and then decreases with further thickening of soil cover (Fig. 5). This pattern of depth-dependent positive and negative feedbacks could reinforce the heterogeneity of weathering rates in the epikarst where soils can penetrate into the carbonate critical zone within fractures and dissolution pits (Williams, 2008). Such epikarst, as defined by Williams (2008), exists within the vadose zone. However, because BICY consists of low-lying eogenetic karst (Vacher and Mylroie, 2002) in which karst underlying wetlands are continuously in the phreatic zone, the epikarst is likely to be more homogeneous resulting in uniform downward weathering than expected in telogenetic epikarst zones or in the vadose zones of epigenetic karst (e.g., Gulley et al., 2013).

The feedback between soil thickness and weathering rate is a basic property related to landform evolution (Phillips et al., 2005). Here we show that critical soil thickness Z_{max}, defined as the soil thickness where the maximum weathering rate occurs, is regulated by the environment (Fig. 5). A low Z_{max} is more likely to be observed in systems with low transport rate (e.g., low groundwater drainage rate, low soil water content). In these systems, a large increase in biogenic CO_2 leads to only a small increase of CO_2 arriving at bedrock. Consequently, in such systems negative relationship between soil CO_2 concentrations and weathering rates are expected to be more common. In contrast, in systems with high vertical transport rate, the positive effect of soil cover is expected to be more prevalent. It may also contribute to distinctively different karst landforms around the world. A large Z_{max} value (that is, positive soil-weathering feedback spans a wide range of soil thickness) is likely to generate features like sinkholes (Baryakh and Fedoseev, 2011) and tower karst (Tang, 2002). Under intermediate condition, the maxima in the soil cover-weathering rate relationship could lead to local bi-stability of soil depth and resulting landforms (D'Odorico, 2000). A low Z_{max} (narrow range of positive feedback) creates geomorphic features in equilibrium with the condition of the system (Phillips, 2005). At geological timescales, concentrations of dissolved weathering products in groundwater may increase (e.g., Edmunds et al., 2002; Macpherson et al., 2008), which would in turn reduce weathering rate (Fig. 1I). Increase in weathering products would also provide a mechanism of reducing weathering rate from bottom up, as shown in this study, and reported elsewhere (e.g., Rempe and Dietrich, 2014).

While the effect of soil cover on weathering is widely recognized (Clair et al., 2015; Brantley et al., 2017; Li et al., 2017), its effects have not been quantified across a broad range of environments. This study provides a framework for estimating soil depth effects on weathering and its dependence on other environmental conditions. First, we show that the first-order effect of soil cover is as significant as that of precipitation (Fig. 4). Moreover, the significant second-order effects (Fig. 4), specifically the interplay between soil cover and other environmental variables, further complicates efforts to assess the effect of soil cover on weathering. Essentially, soil transport rate and path length from acid sources to reaction sites modify the effect of soil cover thickness in different environments (Fig. 5). Significant second-order effects presented by many environmental variables (Fig. 4) may partly explain the large variation and sometimes even contradictory results in the effect of individual variables reported in literature (e.g., Moulton and Berner, 1998; Bormann et al., 1998; Gaillardet et al., 1999; Oliva et al., 2003). This finding suggests that predictions of weathering rate and solute export at broad spatial scales would be improved by mechanistic models, such as the one presented here, that account for these interactions.

In conclusion, landscapes evolve in response to external forces, such as tectonics and climate that influence surface processes of erosion and weathering. Internal biogeomorphic and ecohydrologic feedbacks in developing landforms, however, play a significant and integral role, with external forces regulating the strength of these feedbacks. Partitioning and evaluating the complex interaction among these processes is essential for efforts to understand and predict the variability in chemical weathering of bedrock in all environments.

Acknowledgements

This project is funded by National Science Foundation award DEB#1354783 (PIs: M.J. Cohen, J.B. Heffernan, D.L. McLaughlin, J.B. Martin and A.B. Murray). This work used the Extreme Science and Engineering Discovery Environment (XSEDE), supported by National Science Foundation grant number ACI-1548562 and high-throughput computation at Duke Research Computing from Duke University. Site access was enabled by the US National Park Service under permit #BICY-2016-SCI-0008. The manuscript greatly benefited from the constructive comments from two anonymous reviewers.

References

Ahnert, F., 1988. Modeling landform change. In: Anderson, M.G. (Ed.), Modeling Geomorphological Systems. John Wiley, New York, pp. 375–400.
Baryakh, A.A., Fedoseev, A.K., 2011. Sinkhole formation mechanism. J. Min. Sci. 47, 404–412.
Berner, R.A., 1978. Rate control of mineral dissolution under earth surface conditions. Am. J. Sci. 278, 1235–1252.
Berner, R.A., 1992. Weathering, plants, and the long-term carbon cycle. Geochim. Cosmochim. Acta 56, 3225–3231.
Berner, R.A., Lasaga, A.C., Garrels, R.M., 1983. The carbonate-silicate geochemical cycle and its effect on atmospheric carbon dioxide over the past 100 million years. Am. J. Sci. 283, 641–683.
Bormann, B.T., et al., 1998. Rapid, plant-induced weathering in an aggrading experimental ecosystem. Biogeochemistry 43, 129–155.
Boucher, D.F., Alves, G.E., 1959. Dimensionless numbers for fluid mechanics, heat transfer, mass transfer and chemical reaction. Chem. Eng. Prog. 55, 55–64.
Brantley, S.L., 2010. Weathering: rock to regolith. Nat. Geosci. 3, 305.
Brantley, S.L., Lebedeva, M.I., Balashov, V.N., Singha, K., Sullivan, P., Stinchcomb, G., 2017. Toward a conceptual model relating chemical reaction fronts to water flow paths in hills. Geomorphology 277, 100–117.
Buhmann, D., Dreybrodt, W., 1985. The kinetics of calcite dissolution and precipitation in geologically relevant situations of karst areas. 1. Open system. Chem. Geol. 53, 109–124.
Carson, M.A., Kirkby, M.J., 1972. Hillslope Form and Process. Cambridge University Press, New York.
Celia, M.A., Bouloutas, E.T., Zarba, R.L., 1990. A general mass-conservative numerical solution for the unsaturated flow equation. Water Resour. Res. 26, 1483–1496.
Chamberlin, C., Bianchi, T.S., Brown, A.L., Cohen, M.J., Dong, X., Flint, M.K., Martin, J.B., McLaughlin, D.L., Murray, A.B., Pain, A., Quintero, C.J., Ward, N.D., Zhang, X.,

Heffernan, J.B., 2018. Mass balance implies Holocene development of a low-relief karst patterned landscape. Chem. Geol. http://dx.doi.org/10.1016/j.chemgeo.2018.05.029. (in review).
Chen, X., Hu, Q., 2004. Groundwater influences on soil moisture and surface evaporation. J. Hydrol. 297, 285–300.
Clair, J.St., Moon, S., Holbrook, W.S., Perron, J.T., Riebe, C.S., Martel, S.J., Harman, C., Shingha, K., Richter, D.d., 2015. Geophyiscal imagining reveals topographic stress control of bedrock weathering. Science 350, 534–538.
D'Odorico, P., 2000. A possible bistable evolution of soil thickness. J. Geophys. Res. Solid Earth 105, 25927–25935.
Donders, T.H., et al., 2005. Mid- to late-Holocene El Nino-southern oscillation dynamics reflected in the subtropical terrestrial realm. Proc. Natl. Acad. Sci. U. S. A. 102, 10904–10908.
Dong, W., Wang, Q., 2013. Modeling soil solute release into runoff and transport with runoff on a loess slope. J. Hydrol. Eng. 18, 527–535.
Drever, J.I., 1994. The effect of land plants on weathering rates of silicate minerals. Geochim. Cosmochim. Acta 58 (10), 2325–2332.
Drever, J.I., Stillings, L.L., 1997. The role of organic acids in mineral weathering. Colloids Surf. A Physicochem. Eng. Asp. 120, 167–181.
Eberl, D.D., 2003. User Guide to RockJock - a Program for Determining Quantitative Mineralogy From X-ray Diffraction Data. No. 2003-78. US Geological Survey.
Edmunds, W.M., Carrillo-rivera, J.J., Cardona, A., 2002. Geochemical evolution of groundwater beneath Mexico City. J. Hydrol. 258, 1–24.
Elderfield, H., 2010. Seawater chemistry and climate. Science 327, 1092–1093.
Gabet, E.J., Edelman, R., Langner, H., 2006. Hydrological controls on chemical weathering rates at the soil-bedrock interface. Geology 34 (12), 1065–1068.
Gaillardet, J., Dupré, B., Louvat, P., Allegre, C.J., 1999. Global silicate weathering and CO_2 consumption rates deduced from the chemistry of large rivers. Chem. Geol. 159 (1-4), 3–30.
van Genuchten, M.T., 1980. A closed-form equation for predicting the hydraulic conductivity of unsaturated soils. Soil Sci. Soc. Am. J. 44, 892–898.
Gerke, H.H., 2006. Preferential flow descriptions for structured soils. J. Plant Nutr. Soil Sci. 169, 382–400.
Gulley, J.D., et al., 2013. Formation of phreatic caves in an eogenetic karst aquifer by CO_2 enrichment at lower water tables and subsequent flooding by sea level rise. Earth Surf. Process. Landf. 38, 1210–1224.
Gulley, J.D., et al., 2015. Heterogeneous distributions of CO_2 may be more important for dissolution and karstification in coastal eogenetic limestone than mixing dissolution. Earth Surf. Process. Landf. 40, 1057–1071.
Halley, R.B., Schmoker, J.W., 1983. High-porosity Cenozoic carbonate rocks of South Florida: progressive loss of porosity with depth. Am. Assoc. Pet. Geol. Bull. 2, 191–200.
Hilley, G.E., Porder, S., 2008. A framework for predicting global silicate weathering and CO_2 drawdown rates over geologic time-scales. Proc. Natl. Acad. Sci. U. S. A. 105, 16855–16859.
Hinsinger, P., et al., 2001. Plant-induced weathering of a basaltic rock: experimental evidence. Geochim. Cosmochim. Acta 65, 137–152.
Huang, K., Mohanty, B.P., van Genuchten, M.T., 1996. A new convergence criterion for the modified Picard iteration method to solve the variably saturated flow equation. J. Hydrol. 178, 69–91.
Jacobson, A.D., Blum, J.D., Walter, L.M., 2002. Reconciling the elemental and Sr isotope composition of Himalayan weathering fluxes: insights from the carbonate geochemistry of stream waters. Geochim. Cosmochim. Acta 66, 3417–3429.
Kelly, E.F., Chadwick, O.A., Hilinski, T.E., 1998. The effect of plants on mineral weathering. Biogeochemistry 42, 21–53.
Kump, L.R., Brantley, S.L., Arthur, M.A., 2000. Chemical weathering, atmospheric CO_2, and climate. Annu. Rev. Earth Planet. Sci. Lett. 28, 611–667.
Laio, F., et al., 2001. Plants in water-controlled ecosystems: active role in hydrologic processes and response to water stress II. Probabilistic soil moisture dynamics. Advance in. Water Res. 24, 707–723.
Lambeck, K., et al., 2014. Sea level and global ice volumes from the last glacial maximum to the Holocene. Proc. Natl. Acad. Sci. 111, 15296–15303.
Li, L., et al., 2017. Expanding the role of reactive transport models in critical zone processes. Earth Sci. Rev. 165, 280–301.
Lietz, A.C., 2000. Analysis of Water-quality Trends at two Discharge Stations-one within Big Cypress National Preserve and one near Biscayne Bay-southern Florida, 1966–94. US Department of the Interior, US Geological Survey.
Liu, Z., Dreybrodt, W., Liu, H., 2011. Atmospheric CO_2 sink: silicate weathering or carbonate weathering? Appl. Geochem. 26, S292–S294.
Lucas, Y., 2001. The role of plants in controlling rates and products of weathering: importance of biological pumping. Annu. Rev. Earth Planet. Sci. 29 (1), 135–163.
Macpherson, G.L., et al., 2008. Increasing shallow groundwater CO_2 and limestone weathering, Konza Prairie, USA. Geochim. Cosmochim. Acta 72, 5581–5599.
Maher, K., 2010. The dependence of chemical weathering rates on fluid residence time. Earth Planet. Sci. Lett. 294, 101–110.
Maher, K., Chamberlain, C.P., 2014. Hydrologic regulation of chemical weathering and the geologic carbon cycle. Science 343 (6178), 1502–1504.
Martin, J.B., 2017. Carbonate minerals in the global carbon cycle. Chem. Geol. 449, 58–72.
Martin, C.E., Francke, S.K., 2015. Root aeration function of Baldcypress knees (Taxodium distichum). Int. J. Plant Sci. 176, 170–173.
May, E.R., Wolfgang, D., 2010. A new direction in effective accounting for the atmospheric CO_2 budget: considering the combined action of carbonate dissolution, the global water cycle and photosynthetic uptake of DIC by aquatic organisms. Earth-Sci. Rev. 99, 162–172.
McLaughlin, D.L., Kaplan, D.A., Cohen, M.J., 2014. A significantly nexus: geographically isolated wetlands influence landscape hydrology. Water Resour. Res. 50, 5329–5333.
Megonigal, J.P., Day, F.P., 1992. Effects of flooding on root and shoot production of bald cypress in large experimental enclosures. Ecology 73, 1182–1193.
Monger, H.C., Daugherty, L.A., Lindmann, W.C., 1991. Microbial precipitation of pedogenic calcite. Geology 19, 997–1000.
Montague, K., Day, F.P., 1980. Belowground biomass of four plant communities of the great dismal swamp, Virginia. Am. Midl. Nat. 103, 83–87.
Moore, T.R., Knowles, R., 1989. The influence of water table levels on methane and carbon dioxide emissions from peatland soils. Can. J. Soil Sci. 38, 33–38.
Moriasi, D.N., Arnold, J.G., Van Liew, N.W., Bingner, R.L., Harmel, R.D., Veith, T.L., 2007. Model evaluation guidelines for systematic quantification of accuracy in watershed simulations. Trans. ASABE 50, 885–900.
Morris, M.D., 1991. Factorial sampling plans for preliminary computational experiments. Technometrics 33, 161–174.
Moulton, K.L., Berner, R.A., 1998. Quantification of the effect of plants on weathering: studies in Iceland. Geology 26, 895–898.
Moulton, K.L., West, J., Berner, R.A., 2000. Solute flux and mineral mass balance approaches to the quantification of plant effects on silicate weathering. Am. J. Sci. 300, 539–570.
Mualem, Y., 1976. A new model for predicting the hydraulic conductivity of unsaturated porous media. Water Resour. Res. 12, 513–522.
Murray, A.N., Love, W.W., 1929. Action of organic acids upon limestone. AAPG Bull. 13, 1467–1475.
Oliva, P., Viers, J., Dupré, B., 2003. Chemical weathering in granitic environments. Chem. Geol. 202, 225–256.
Pelletier, J.D., Rasmussen, C., 2009. Quantifying the climatic and tectonic controls on hillslope steepness and erosion rate. Lithosphere 1, 73–80.
Petuch, E.J., Roberts, C.E., 2007. The Geology of the Everglades and Adjacent Areas. CRC Press, Boca Raton FL.
Phillips, J.D., 2005. Weathering instability and landscape evolution. Geomorphology 67, 255–272.
Phillips, J.D., 2016. Biogeomorphology and contingent ecosystem engineering in karst landscapes. Prog. Phys. Geogr. 40, 503–526.
Phillips, J.D., et al., 2005. Nonequilibrium regolith thickness in the Ouachita Mountains. J. Geol. 113, 325–340.
Plummer, L.N., Wigley, T.M.L., Parkhurst, D.L., 1978. The kinetics of calcite dissolution in CO2-water systems at 5C to 60C and 0.0 to 1.0 atm CO_2. Am. J. Sci. 278, 179–216.
Quade, J., English, N., DeCelles, P.G., 2003. Silicate versus carbonate weathering in the Himalaya: a comparison of the Arun and Seti River watersheds. Chem. Geol. 202 (3-4), 275–296.
Rasmussen, C., et al., 2011. An open system framework for integrating critical zone structure and function. Biogeochemistry 102, 15–29.
Rempe, D.M., Dietrich, W.E., 2014. A bottom-up control on fresh-bedrock topography under landscapes. Proc. Natl. Acad. Sci. U. S. A. 111, 6576–6581.
Riebe, C.S., Kirchner, J.W., Finkel, R.C., 2004. Erosional and climatic effects on long-term chemical weathering rates in granitic landscapes spanning diverse climate regimes. Earth Planet. Sci. Lett. 224, 547–562.
Ross, M.S., O'Brien, J.J., da Silveira Lobo Sternberg, L., 1994. Sea-Level Rise and the Reduction in Pine Forests in the Florida Keys. Ecol. Appl. 4 (1), 144–156.
Saltelli, A., Tarantola, S., Campolongo, F., Ratto, M., 2004. Sensitivity Analysis in Practice: A Guide to Assessing Scientific Models. Probability and Statistics Series John & Sons publishers.
Scanlon, B.R., Nicot, J.P., Massmann, J.W., 2002. Soil gas movement in unsaturated systems. In: Warrick, A.W. (Ed.), Soil Physics Companion. CRC Press, Boca Raton, FL.
Simunek, J., Suarez, D.L., 1993. Modeling of carbon-dioxide transport and production in soil.1. Model development. Water Resour. Res. 29, 487–497.
Steefel, C.I., Maher, K., 2009. Fluid-Rock Interaction: A Reactive Transport Approach.
Sullivan, P.L., et al., 2012. The role of recharge and evapotranspiration as hydraulic drivers of ion concentrations in shallow groundwater on Everglades tree islands, Florida (USA). Hydrol. Process. 28, 293–304.
Tang, T., 2002. Surface sediment characteristics and tower karst dissolution, Guilin, southern China. Geomorphology 49, 231–254.
Torres, M.A., West, A.J., Li, G., 2014. Sulphide oxidation and carbonate dissolution as a source of CO_2 over geological timescales. Nature 507, 346–349.
Vacher, H.L., Mylroie, J.E., 2002. Eogenetic karst from the perspective of an equivlent porous medium. Carbonates Evaporites 17, 182–196.
Watts, W.A., Hansen, B.C.S., 1994. Pre-Holocene and Holocene pollen records of vegetation history from the Florida peninsular and their climatic implications. Palaeogeogr. Palaeoclimatol. Palaeoecol. 109, 163–176.
Watts, A.C., Kobziar, L.N., Snyder, J.R., 2012. Fire reinforces structure of pondcypress (*taxodium distichum* var. imbricarium) domes in a wetland landscape. Wetlands 32, 439–448.
Watts, A.C., et al., 2014. Evidence of biogeomorphic patterning in a low-relief karst landscape. Earth Surf. Process. Landf. 39, 2027–2037.
West, A.J., Galy, A., Bickle, M., 2005. Tectonic and climatic controls on silicate weathering. Earth Planet. Sci. Lett. 235, 211–228.
White, A.F., Blum, A.E., 1995. Effects of climate on chemical weathering in watersheds. Geochim. Cosmochim. Acta 59 (9), 1729–1747.
Williams, P.W., 2008. The role of the epikarst in karst and cave hydrogeology: a review. Int. J. Speleol. 37, 1–10.
Woo, M., Marsh, P., 1976. Effect of vegetation on limestone solution in a small High Arctic basin. Can. J. Earth Sci. 14, 571–581.
Xiang, L., et al., 2012. Evaluating coupled water, vapor, and heat flows and their influence on moisture dynamics in arid regions. J. Hydrol. Eng. 17, 565–577.
Zeng, Y., et al., 2011. Numerical analysis of air - water - heat flow in unsaturated soil: is it necessary to consider airflow in land surface models? J. Geophys. Res. 116, 1–18.